

THE UNIVERSITY OF CALGARY

Planar Electrode Dielectrophoresis Systems

by

Lee Fason Hartley

A THESIS

SUBMITTED TO THE FACULTY OF GRADUATE STUDIES
IN PARTIAL FULFILLMENT OF THE REQUIREMENTS FOR THE
DEGREE OF MASTER OF SCIENCE

DEPARTMENT OF ELECTRICAL AND COMPUTER ENGINEERING

CALGARY, ALBERTA

SEPTEMBER, 1997

© Lee Fason Hartley 1997



National Library
of Canada

Acquisitions and
Bibliographic Services

395 Wellington Street
Ottawa ON K1A 0N4
Canada

Bibliothèque nationale
du Canada

Acquisitions et
services bibliographiques

395, rue Wellington
Ottawa ON K1A 0N4
Canada

Your file *Votre référence*

Our file *Notre référence*

The author has granted a non-exclusive licence allowing the National Library of Canada to reproduce, loan, distribute or sell copies of this thesis in microform, paper or electronic formats.

The author retains ownership of the copyright in this thesis. Neither the thesis nor substantial extracts from it may be printed or otherwise reproduced without the author's permission.

L'auteur a accordé une licence non exclusive permettant à la Bibliothèque nationale du Canada de reproduire, prêter, distribuer ou vendre des copies de cette thèse sous la forme de microfiche/film, de reproduction sur papier ou sur format électronique.

L'auteur conserve la propriété du droit d'auteur qui protège cette thèse. Ni la thèse ni des extraits substantiels de celle-ci ne doivent être imprimés ou autrement reproduits sans son autorisation.

0-612-24718-X

Canada

ABSTRACT

Demand from the biosciences continues to increase for systems able to assist in the preparation and analysis of biological samples. Appropriately, dielectrophoresis continues to emerge as a valuable technique for characterizing a diverse array of particles. Particle processing systems capable of autonomously executing various operations on samples may offer cost effective means for such tasks. Dielectrophoretic microelectromechanical systems technology is well positioned to participate in this growing industry.

Dielectrophoresis is an effective means for micro-particle manipulation, but the mechanical structures required for such work are typically cost prohibitive in volumes. For dielectrophoretic particle processors to be competitive, MEMS technology must be leveraged to provide useful functions at reasonable costs.

This thesis will study three dielectrophoretic structures that are candidates for integration into planar processing systems. The dielectrophoretic function of each component will first be analytically described. Then a discrete planar electrode model will be derived and characterized using boundary element method simulation. Lastly, experimental levitation data from a fabricated discrete planar quadrupole device will be used to validate analytical theory.

ACKNOWLEDGEMENTS

In completing the work comprised herein, the invaluable assistance of several people must be noted. First and foremost, my supervisor Dr. Karan Kaler assisted my progress not only with his thorough technical command of the field, but also with his personal guidance, support and friendship. I would also like to extend my gratitude to Dr. Reginald Paul of the Department of Chemistry for his essential assistance on mathematical matters.

Financial, fabrication and personnel contributions from the Alberta Microelectronics Center in Edmonton were also of paramount importance. Specifically I express my gratitude to Dr. Yuebin Ning (my industrial advisor) and Dr. Graham McKinnon for their technical input on fabrication issues.

The financial success of my program relied on the generous support of the University of Calgary Department of Electrical and Computer Engineering through their provision of various graduate scholarships and teaching assistantships. In conjunction with this support, an NSERC Post Graduate Industrial Scholarship through the Alberta Microelectronics Center made the personal aspects of student family life possible.

My deepest acknowledgements are extended lovingly to my wife, Allison, whose support, love and understanding makes anything possible. Lastly, whilst being physically the smallest recipient of my gratitude, my daughter Paige receives a disproportionately large appreciation for the joy she brings to my world.

DEDICATION

To family and friends who have always supported my efforts.

TABLE OF CONTENTS

Approval Page	ii
Abstract.....	iii
Acknowledgements.....	iv
Dedication.....	v
Table of Contents.....	vi
List of Tables	viii
List of Figures.....	ix
List of Graphs	xi
List of symbols	xii
Introduction.....	1
The Macroscopic Polarization of Matter	4
Dielectrophoresis	8
Fundamentals of the DEP Force	8
Positive vs Negative Dielectrophoresis	11
Dipole Levitation Theory	15
Quadrupole Levitation Theory	16
Isomotive Theory.....	18
Electrostatic Simulation.....	22
Finite Difference Method	22
Finite Element Method	23
Boundary Element Method.....	24

BEM Simulation Results	26
Dipole Levitator Simulation	26
Quadrupole Simulation	38
Isomotive Simulation	41
Experimental Work	45
The Discrete Planar Quadrupole Device	45
Numerical Modeling of the Planar Quadrupole Device	47
Discrete Planar Quadrupole Chamber Assembly	50
Setup of the Experimental Fluid Circuit	53
Particle Capture	55
Hydrodynamic Particle Rolling	56
Levitation Data	58
Sources of Error	66
Conclusions	69
Summary of Accomplishments	69
Problems Encountered	71
Directions for Future Work	72
Appendices	77
Mechanical Drawings	77
References	81

LIST OF TABLES

Table 1 - Properties of Levitated Particles.....	60
--	----

LIST OF FIGURES

Figure 1 – Normal Electric Field Boundary Condition at Dielectric Interface.....	6
Figure 2 – Equivalent Dipole Polarization.....	9
Figure 3 - DEP Force From Energy Principles.....	13
Figure 4 – Typical Dipole Levitator Architecture	16
Figure 5 –The Point Charge Quadrupole Model.....	17
Figure 6 – An Isomotive Electrode System (Sectional View).....	21
Figure 7 – The Finite Line Charge Over Ground Model	28
Figure 8 - Coulomb Representation of Finite Line Charge	32
Figure 9 - Discrete Planar Representation of Cone-Plate Dipole Levitator.....	34
Figure 10 - Coulomb Model of Discrete Planar Dipole Levitator	35
Figure 11 - Enhanced Discrete Planar Dipole Levitator	37
Figure 12 – The Discrete Planar Isomotive Electrode System	43
Figure 13 - Laboratory Equipment Arrangement	45
Figure 14 - AMC Quadrupole Chiplet	46
Figure 15 - The Equivalent Point Charge Quadrupole	49
Figure 16 - Quadrupole Fluid Integrated Circuit Chamber – Front X-Section.....	50
Figure 17 – Optical View for Chamber Housing Alignment.....	51
Figure 18 – Experimental Fluid Circuit.....	54
Figure 19 - Quadrupole Chamber Mounted in Optical System	56
Figure 20 - A Particle Misaligned to the Quadrupole Region	57
Figure 21 - Fluid Circuit Hydro Dynamics.....	58

Figure 22 - Typical Levitation Images (a-c) plus 10 μ m Scale (d).....	59
Figure 23 - Discrete Planar Isomotive Chip	70
Figure 24 - Isomotive Separation Chamber	70
Figure 25 – Proposed MEMS Quadrupole Injection System.....	75
Figure 26 - Front View of Microscope Chamber Stage.....	77
Figure 27 - Side View of Microscope Chamber Stage	78
Figure 28 - Ealing Optics (x,y,z) Adjust Assembly	79
Figure 29 - Lead Carrier Assembly Prior to Housing Attachment	79
Figure 30 - Assembled Chamber Housing.....	80

LIST OF GRAPHS

Graph 1 - F_{DEP} as Function of Line Charge Length.....	30
Graph 2 – Positional Dependence of F_{DEP}/r^3 in Finite Line Charge Model.....	32
Graph 3 – Particle Radius Extraction from Line Charge Simulation	33
Graph 4 - Discrete Planar Dipole Levitator Performance.....	36
Graph 5 – Positional Dependence of Quadrupolar Levitation Force.....	39
Graph 6 – Particle Radius Extraction from Quadrupole Simulation	40
Graph 7 - Normalized Discrete Isomotive Force Spectrum.....	44
Graph 8 –Discrete Planar Quadrupole Force Profiles.....	47
Graph 9 - Point Charge Representation of Discrete Planar Quadrupole	48
Graph 10 - Normalized Experimental Spheriglass Force Profiles.....	62
Graph 11 - Spheriglass Experimental Radius Extraction	64
Graph 12 - Normalized Experimental Polyethylmethacrylate Force Profiles	65
Graph 13 - Polyethylmethacrylate Experimental Radius Extraction.....	66

LIST OF SYMBOLS

Operators:

- ∇ gradient (del) operator
 $|\cdot|$ absolute value
 $\text{Re}[\cdot]$ real part of complex number
 $\text{Im}[\cdot]$ imaginary part of complex number

Symbols:

- ϵ_0 permittivity of free space (8.854×10^{-12} F/m)
 ϵ^* complex permittivity
 ϵ' effective permittivity
 ϵ_p particle permittivity
 ϵ_m media permittivity
 σ^* complex conductivity
 σ' effective conductivity (mho/m)
 σ_p particle conductivity
 σ_m media conductivity
 ξ complex dielectric factor
 G conductance (mho)
 α volume polarizability
 v particle volume
 C capacitance (Farads)

E	electric field strength (volts/meter)
V	scalar electrical potential (volts)
I	electric current (coulombs/second)
j	$\sqrt{-1}$
ω	angular frequency (radians/second)
f	frequency (Hz)
q	free charge (coulombs)
Q_s	surface charge density (coulombs/meter ²)
λ	line charge density (coulombs/meter)
z	vertical position in frame of reference
ρ	radial position in cylindrical coordinates
r	particle radius
K_n	polarization coefficient
K_1	Dipolar polarization coefficient (Clausius-Mosotti)
K_2	Quadrupolar polarization coefficient

INTRODUCTION

Science has long pursued an understanding of the electrical properties of materials, and repeatedly the search unearths both novel applications as well as new and increasingly complex questions. Consider the biological sciences. Their pursuit of the mechanisms of life have led to astonishing discoveries that by and large have benefited humankind tremendously. Science can place a criminal at the scene of a crime from a microscopic genetic signature, it can manipulate complex metabolic pathways to ward off illnesses and an entire organism may now be cloned from a molecular 'original'.

Whilst science wields such powerful abilities, it is important to remember that nature is still ultimately in command. Diseases such as acquired immune deficiency syndrome and cancer continue to claim victims, and bacterial adaptation yields strains able to withstand medicine's most powerful drugs. Humankind's desire to study, understand and ultimately control the environment in which we live is an evolutionary advantage to our species. We have ascended the natural order to become the ultimate macroscopic predator, but foes from the microscopic realm of our world increasingly pose the greatest threats. To defend against these viral and microbial threats, cross discipline efforts must be increasingly undertaken to further unravel their mysteries.

Cellular physiology and biochemical mechanisms are of paramount significance in the pursuit of biological understanding, and an immensity of information in these fields remains unexplained. In an organism of even moderate complexity, the diversity of function exhibited by the composite classes of cells and biomolecules can be staggering. From a microbiological point of view, much is known about the physical and chemical

makeup of simple cells. Theories of symbiotic cellular evolution offer explanations for the 'cell within a cell' appearance of mitochondria, the fluid mosaic model depicts a highly specialized cellular membrane comprised of emulsified globular proteins in a lipid bilayer and polymer biochemistry provides mechanistic foundations for cellular division.

While many areas of biological understanding are advanced, others like the electrical properties of a cell, remain in their infancy. One may ask what are the solutions to Maxwell's equations throughout a living cell? How do changes in cellular physiology and structure affect this electrical makeup? How do externally imposed electromagnetic fields influence the physiological state of a cell? To effectively address questions such as these, methods for modeling various hypotheses are required, and subsequent experimentation must be performed to support or refute the hypothesis. While such a process is characteristic of the scientific method, the tools required to complete the cycle in the biological laboratory are not necessarily available.

The physical sizes of specimens and the specialized chambers in which these specimens must be placed increasingly demand manufacturing precision and scale characteristic of the microelectronics industry. Unfortunately, as the complexity of both the test devices and the specimens increase, analytical solutions to the electrostatic systems become evasive. Simulation tools must therefore be employed to augment the mathematician's analytical solution as the theoretical benchmarks to experimental data.

Simulation packages implementing various numerical methods have experienced widespread acceptance across a variety of scientific disciplines for decades. Algorithms including the finite difference method (FDM), finite element method (FEM) and the boundary element method (BEM) have offered scientists iterative answers to problems

which are too complex for analytical solution. Rapid growth in the area of microelectromechanical systems (MEMS) design has begun to provide a new and unique set of problems for these simulators to tackle. Dielectrophoretic MEMS is one technology that will increasingly rely on numerical simulation.

Dielectrophoresis , or DEP, deals with the behavior of neutral matter in non-linear electric fields. The frequency dependent dielectrophoretic spectrum is determined by particle geometry, the degree of non-linearity in the applied electric field and the relative polarizabilities of the particle and the surrounding media. With its roots in Maxwell's equations, dielectrophoresis experimentation offers valuable insight into the electrical makeup of materials.

This thesis aims to stimulate continued development of cost effective devices capable of automating a wide range of analytical laboratory tasks. Applying precision microelectronics technology, MEMS, boundary element method (BEM) electrostatic modeling and traditional dielectrophoresis theory, an economical set of planar electrode devices have been assembled.

$$C = \frac{C_o \epsilon'}{\epsilon_o} \quad (4)$$

An out-of-phase current (I_c) will lead the applied voltage (V) by 90 degrees as given by

$$I_c = j\omega CV = j\omega \epsilon' \frac{C_o V}{\epsilon_o} \quad (5)$$

The non-ideal dielectric media will also possess a finite conductivity (σ') giving rise to a conductance

$$G = \frac{\sigma' A}{d} = \frac{C_o \sigma'}{\epsilon_o} \quad (6)$$

resulting in an in-phase current

$$I_R = GV = \sigma' \frac{C_o V}{\epsilon_o} \quad (7)$$

The total capacitor current (I_T) can now be expressed as the sum of I_C and I_R

$$I_T = j\omega[\epsilon' - j\sigma'/\omega] \frac{C_o V}{\epsilon_o} = j\omega \epsilon^* \frac{C_o V}{\epsilon_o} \quad (8)$$

where ϵ^* is the complex permittivity of (1).

While such an analysis is useful in developing an intuitive appreciation for the interrelation of polarization and conduction, it must be noted that these results are merely an implicit representation of the true conduction and polarization mechanisms governed by Maxwell's equations. A rigorous analysis of the subject of polarization yields the *complex dielectric factor* [1]

$$\xi = \epsilon^* - j\sigma^*/\omega \quad (9)$$

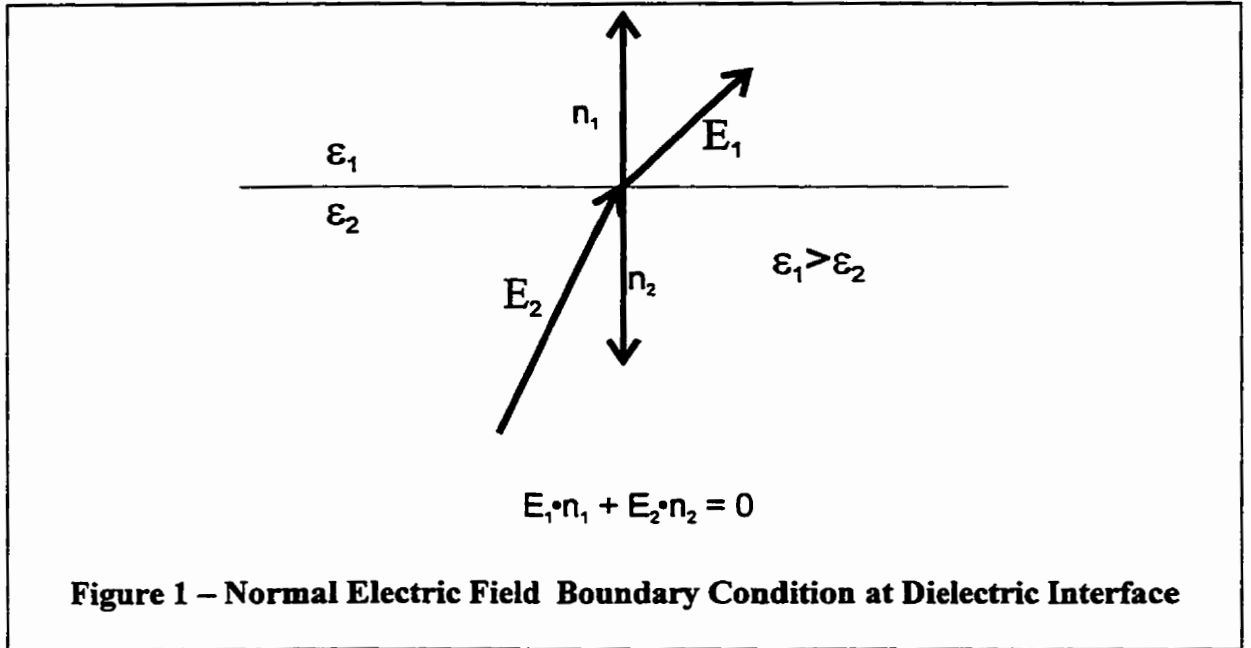
where ε^* and σ^* are the complex dielectric constant and complex conductivity respectively. The complex dielectric factors (ξ_1, ξ_2) describe the electric field boundary conditions for joined media as

$$\xi_1(\vec{n}_1 \cdot \vec{E}_1) + \xi_2(\vec{n}_2 \cdot \vec{E}_2) = 0 \quad (10)$$

For ideal dielectrics, this relationship reduces to the familiar

$$\varepsilon_1(\vec{n}_1 \cdot \vec{E}_1) + \varepsilon_2(\vec{n}_2 \cdot \vec{E}_2) = 0 \quad (11)$$

condition for electric fields across dielectric boundaries shown in Figure 1.



The purpose of this work is not to study Maxwell's polarization equations, but rather to characterize apparatus capable of achieving dielectrophoretic particle manipulation. The discussion herein simply serves to highlight the permittivity, conductivity and

frequency dependencies which are fundamentally part of the electric polarization response of matter.

DIELECTROPHORESIS

A useful starting point in developing an understanding of dielectrophoresis is to contrast it with the more widely known electrophoresis. The motion of charged bodies in the presence of electric fields (uniform or non-uniform) is described by electrophoresis. Dielectrophoresis, on the other hand, characterizes the behavior of polarizable matter in the presence of non-uniform electric fields. Stated another way, electric fields of any configuration will exert a Coulombic force on any charged body subjected to the field (electrophoresis), but for a neutral body to experience a net force (dielectrophoresis), the applied electric field must be non-uniform. The dielectrophoretic force is also distinguished by the fact that its direction is independent of the electric field's instantaneous polarity, thereby allowing variable frequency AC sources to be used.

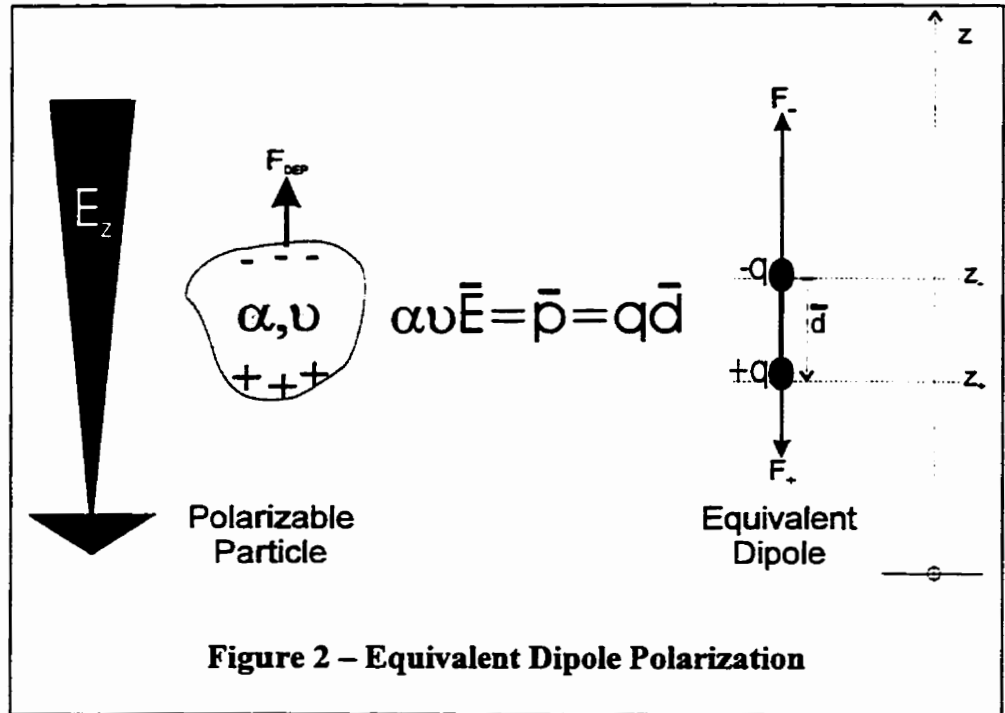
Fundamentals of the DEP Force

To derive the dielectrophoretic force, one may consider a small dielectric body of volume (v) and polarizability (α) exposed to a z -aligned electric field $\vec{E}(z)$ as shown in Figure 2. The net dipole moment induced in the body will then be

$$\vec{p} = \alpha v \vec{E} \quad (12)$$

This polarization may be equivalently represented by two charges ($\pm q$), separated by a distance d such that

$$\vec{p} = q \vec{d} \quad (13)$$



To assess the total force exerted on the body, the coulombic force exerted on each end of the equivalent dipole is considered. The charge $+q$ experiences

$$\vec{F}_+ = q\vec{E}(z_+) \quad (14)$$

while the charge $-q$ experiences

$$\vec{F}_- = -q\vec{E}(z_-) \quad (15)$$

Requiring that the equivalent dipole dimension (d) be small, the first two terms of a Taylor series expansion of E_z about z yields

$$\vec{E}(z_+) = \vec{E}(z_-) + \vec{d}\left(\frac{\partial \vec{E}}{\partial z}\right) \quad (16)$$

Substituting (16) into (14) and summing the result with (15), the net force on the dipole becomes

$$\vec{F}_{net} = q\vec{d}(\partial E / \partial z) = (p_z \partial / \partial z)\vec{E} \quad (17)$$

With this result in mind, examination of Figure 2 confirms that the net force on the dipole would be in the positive z -direction:

- the polarization (p) is in the negative z -direction, i.e. $p_z < 0$
- E is in negative z -direction with increasing magnitude in the positive z -direction, i.e. $\partial E_z / \partial z < 0$

While this example is simplistic in its geometry, the analysis lends itself to expansion in the Cartesian system to the general dipolar expression

$$\vec{F} = (p_x \partial / \partial x + p_y \partial / \partial y + p_z \partial / \partial z)\vec{E} = (\vec{p} \cdot \nabla)\vec{E} \quad (18)$$

Expanding the vector operator ($\vec{p} \cdot \nabla$) with the vector identity

$$(\vec{p} \cdot \nabla)\vec{E} = \nabla(\vec{p} \cdot \vec{E}) - (\vec{E} \cdot \nabla)\vec{p} - \vec{p} \times (\nabla \times \vec{E}) - \vec{E} \times (\nabla \times \vec{p}) \quad (19)$$

and dropping the curl terms, the force reduces to

$$\vec{F} = (\vec{p} \cdot \nabla)\vec{E} = \nabla(\vec{p} \cdot \vec{E}) - (\vec{E} \cdot \nabla)\vec{p} \quad (20)$$

Substituting (12) into this expression and rearranging yields

$$\vec{F} = \alpha v (\vec{E} \cdot \nabla)\vec{E} = \alpha v \nabla |\vec{E}|^2 - \alpha v (\vec{E} \cdot \nabla)\vec{E} \quad (21)$$

from which, upon simplification, the dipolar dielectrophoretic force can be simply expressed by:

$$\vec{F} = \frac{1}{2} \alpha v \nabla |\vec{E}|^2 \quad (22)$$

The dielectrophoretic force responds to the polarizability of the material (α), the volume (v) and the gradient of the square of the electric field. The dependence on the square of the electric field gives the dielectrophoretic force independence from instantaneous field polarity. In the presence of AC fields therefore, the force will be a time averaged force.

The precise polarization in a body depends on the complex permittivities of the particle and the surrounding media as well as the geometry of the particle. A homogeneous sphere of radius r and complex permittivity ϵ_p^* immersed in a media with complex permittivity ϵ_m^* and exposed to an electric field, will undergo polarization according to the Claussius-Mosotti polarization coefficient

$$K_1 = \frac{\epsilon_p^* - \epsilon_m^*}{\epsilon_p^* + 2\epsilon_m^*} \quad (23)$$

resulting in a net dipolar dielectrophoretic force being exerted on the sphere of

$$\vec{F}_{DEP} = 2\pi\epsilon_m r^3 \text{Re}[K_1] \nabla E^2 \quad (24)$$

This formulation quantifies the dependencies on particle volume (r^3), polarizability (K_1) and the gradient of the electric field squared (∇E^2).

Positive vs Negative Dielectrophoresis

For the homogeneous sphere, the Claussius-Mosotti factor (23) is of fundamental importance in the determination of the dielectrophoretic force. Considering this function in the absence of particle and media conductivities, the complex permittivities ($\epsilon_p^*, \epsilon_m^*$)

reduce to the dielectric constants (ϵ_p, ϵ_m) and the Claussius-Mosotti factor becomes the real number expression

$$k_1 = \frac{\epsilon_p - \epsilon_m}{\epsilon_p + 2\epsilon_m} \quad (25)$$

Now imagining a nylon sphere of permittivity 4 immersed into two media: first, water of permittivity 80, and second, air of permittivity 1. Evaluating k_1 for these two scenarios

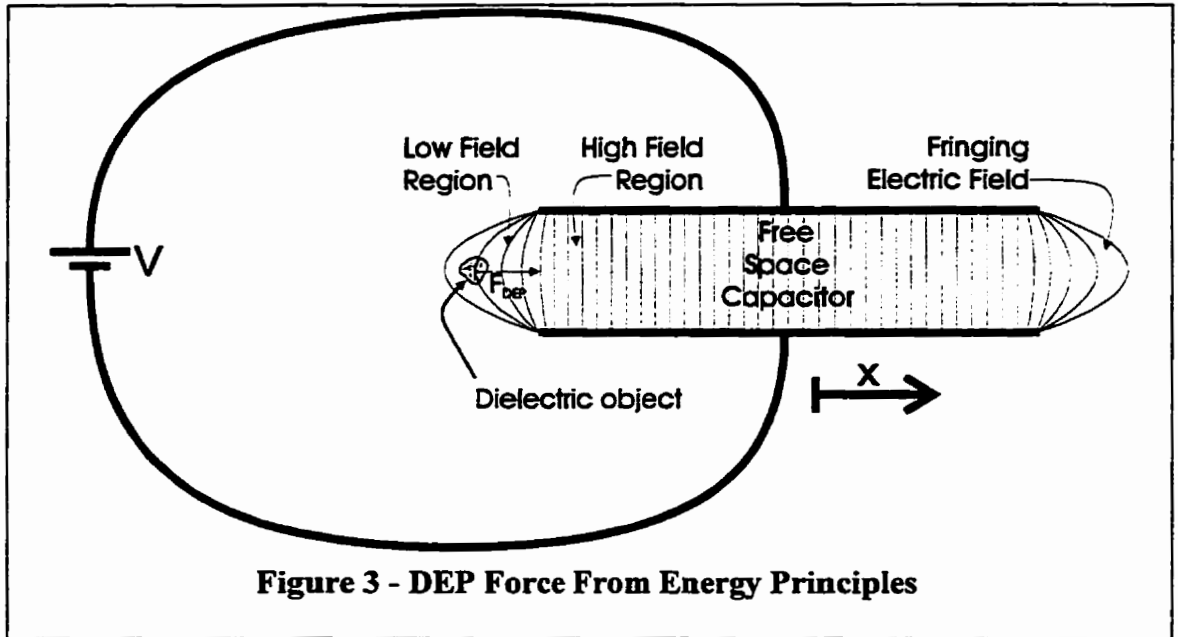
yield $k_{H_2O} = -\frac{76}{164} \cong -0.5$ and $k_{air} = \frac{3}{6} = 0.5$. The sign reversal indicates that (all other

things being equal) the direction of the dielectrophoretic force would be reversed for the two materials. This observation highlights the two distinct modes of dielectrophoresis: negative and positive. Negative dielectrophoresis (the nylon ball in water) tends to eject lower permittivity particles from high field regions; they will be forced opposite the gradient of the E-field squared. Positive dielectrophoresis (the nylon ball in air) results in objects of higher permittivity displacing media of lower permittivity from regions of greater electric field strength. The Claussius-Mosotti factor, being in reality frequency dependent, gives rise to a particle's characteristic dielectrophoretic spectra whereby positive dielectrophoresis can be observed at one frequency, while negative dielectrophoresis is demonstrated by the same particle at another frequency.

An alternative approach to validating the dielectrophoretic phenomenon can be understood from simple energy principles [25]. Consider the parallel plate capacitor shown in Figure 3. Conservation of energy for the system shown in Figure 3 can be stated by

$$\Delta W_{Mechanical} + \Delta W_{Electrical} = \Delta W_{Battery} \quad (26)$$

denoting mechanical, electrical and battery energies respectively. If the dielectric object in Figure 3 is allowed to move by a small distance Δx closer to the parallel plates, the total capacitance of the parallel plate capacitor will increase by an amount ΔC . For the



battery to maintain a constant voltage across the now slightly larger capacitor, an additional amount of charge

$$\Delta Q = (\Delta C)V \quad (27)$$

must be deposited on the capacitor plates thereby increasing the stored electrical energy of the capacitor by

$$\Delta W_{\text{Electrical}} = \Delta W = \frac{1}{2}(\Delta Q)V \quad (28)$$

The battery, on the other hand, having moved the additional charge ΔQ through its potential V will have supplied an amount of energy

$$\Delta W_{\text{Battery}} = (\Delta Q)V = 2\Delta W \quad (29)$$

which is observed to be twice the additional electrical energy now stored in the capacitor. Half of the energy supplied by the battery manifested itself as stored electrical energy in the capacitor whereas the other half of the supplied energy must have gone to mechanical work required to change the capacitance by ΔC .

Now, substitution of (28) and (29) into (26) results in

$$\Delta W_{\text{Mechanical}} = \Delta W \quad (30)$$

which may be rearranged using the relationship

$$\Delta W_{\text{Mechanical}} = F_{\text{DEP}} \Delta x \quad (31)$$

to yield

$$F_{\text{DEP}} = \frac{\Delta W}{\Delta x} = \left. \frac{\partial W}{\partial x} \right|_V = \left. \frac{\partial}{\partial x} \left(\frac{1}{2} CV^2 \right) \right|_V \quad (32)$$

The system of Figure 3 would tend to pull the dielectric object into the capacitor thereby *increasing the capacitance of the system*. This phenomenon is demonstrative of positive dielectrophoresis. Conversely, the same analysis applied to a water dielectric capacitor can be used to predict negative dielectrophoresis on a object of relative permittivity lower than that of water. For the total capacitance of the structure to increase (as constant voltage energy principles dictate), the lower dielectric particle must be repelled from the capacitor region.

Dipole Levitation Theory

Numerous investigators [16,17,33] have demonstrated the ability of axially symmetric electrode structures to achieve levitation of individual particles. A common configuration used to implement a dipole levitation system is the cone-plate assembly of Figure 4b whereby a rounded cone electrode is brought into close proximity to a conducting ground plane. The potential due to this structure is derived from the analytical solution for the electrostatic potential due to a semi-infinite line charge over a ground plane (Figure 4a) which can be shown [38] to be

$$V = \frac{\lambda}{4\pi\epsilon} \ln \left[\frac{h+z + \sqrt{(h+z)^2 + \rho^2}}{h-z + \sqrt{(h-z)^2 + \rho^2}} \right] \quad (33)$$

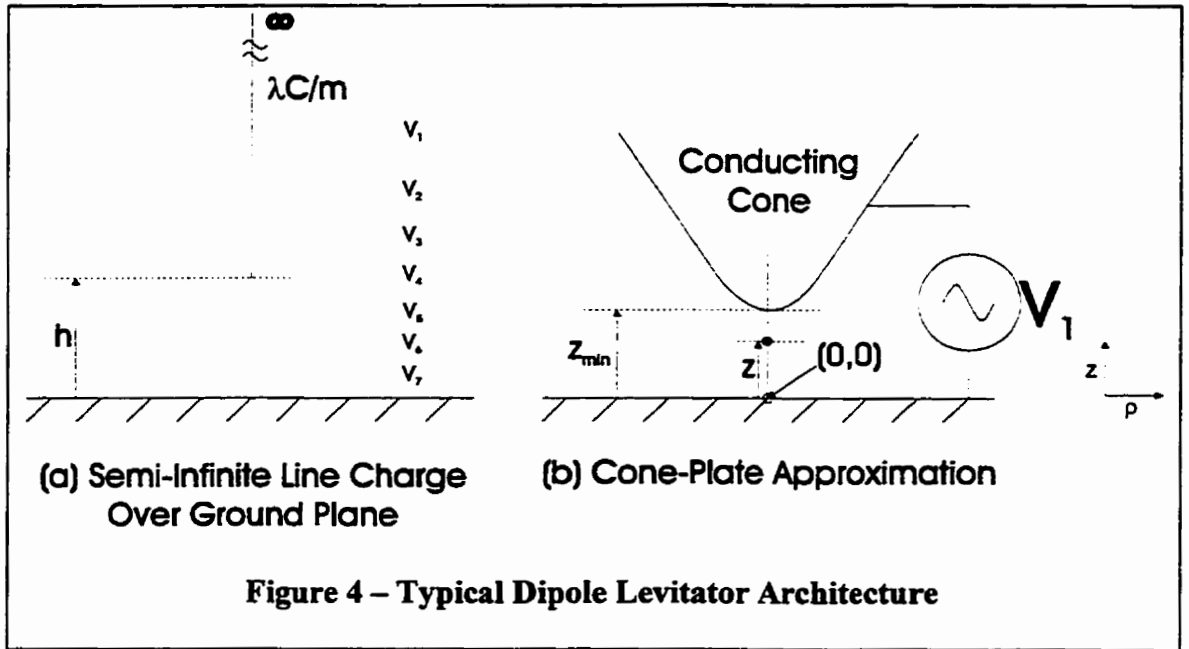
The equipotential surfaces of this scalar field take the form of rounded cones and define the curvature of the conducting tip used for experimentation. Also from the voltage equation (33), the electric field along the z-axis

$$E_z|_{\rho=0} = - \left. \frac{\partial V}{\partial z} \right|_{\rho=0} \quad (34)$$

is determined and the gradient of its square can easily be shown to be

$$\begin{aligned} \frac{\partial E_z^2}{\partial z} &= \frac{\lambda^2}{2\pi^2 \epsilon_m^2} \frac{2h^2 z}{(h^2 - z^2)^3} \\ &= \frac{\lambda^2}{2\pi^2 \epsilon_m^2} G_\infty(z) \end{aligned} \quad (35)$$

where the notation $G_\infty(z)$ is adopted to collect geometric dependencies and the subscript ∞ is meant to indicate a semi-infinite line charge. The ∇E^2 term in the dipolar dielectrophoretic force expression of (24) is now analytically defined. Upon substitution

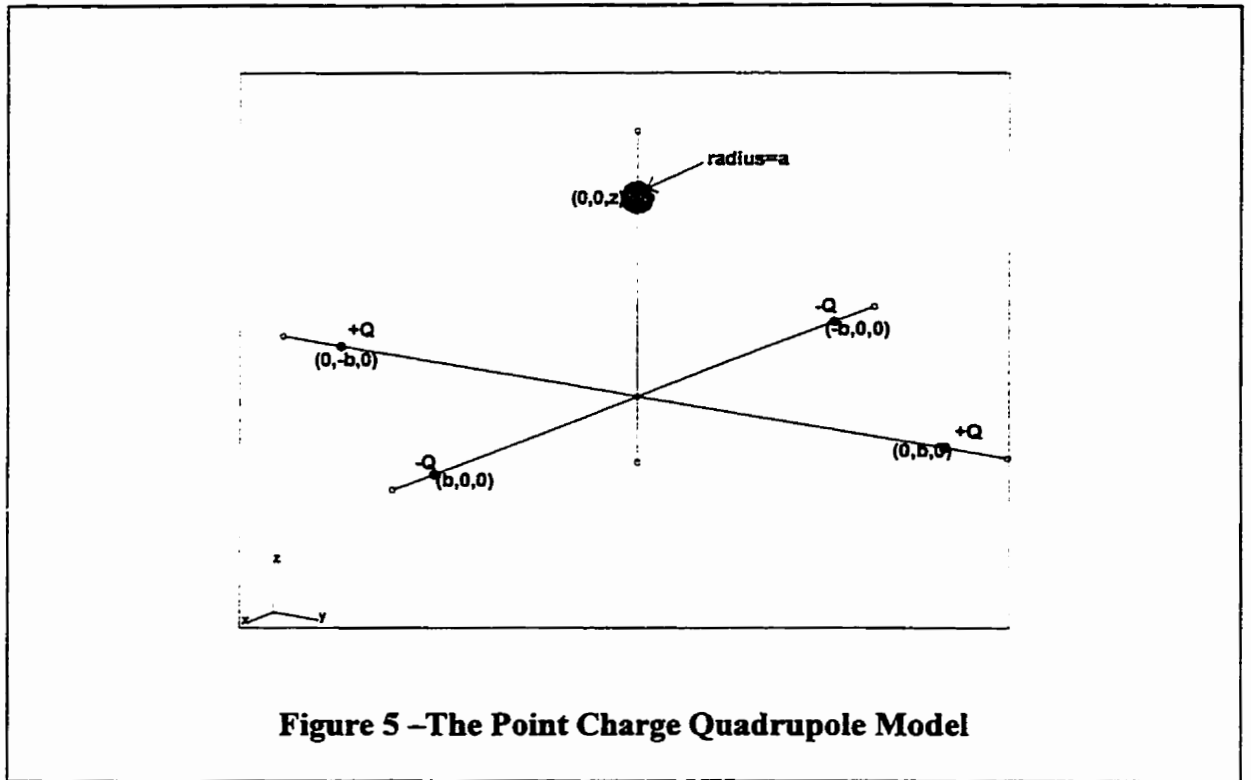


and normalization by r^3 , the force on a homogeneous sphere centered at $(z, 0)$ in Figure 4b becomes

$$\frac{F_{\infty}}{r^3} = \frac{\lambda^2}{\pi\epsilon_m} \text{Re}[K_1] G_{\infty}(z) \quad (36)$$

Quadrupole Levitation Theory

Multipolar moment dielectrophoretic quadrupole theory [2,3,13] enlists a Legendre polynomial expansion in spherical coordinates of the potential due to an azimuthally symmetric arrangement of point charges. The theory predicts a quadrupolar dielectrophoretic force proportional to the 5th power of a particle's radius. Quadrupole levitation is but one application to emerge from this enhanced theory. The quadrupole levitator comprises an azimuthally symmetric electrode arrangement capable of sustaining passive stable particle levitation. The model used for analytical analysis of



quadrupole behavior comprises four point charges (two $+Q$ and two $-Q$) arranged as shown in Figure 5. The quadrupole itself is comprised of the 4 point charges distributed with azimuthal symmetry about the z -axis.

From the generalized expression in spherical coordinates for the potential (Φ_p) at some point (r, θ, ϕ) due to a point charge Q located at (r', θ', ϕ') , superposition is applied to determine the electrostatic potential in the vicinity of the quadrupole. A mathematical extension of the effective dipole method to the effective multipolar moment method [2] is used to determine the force on a vanishingly small sphere with a surface charge distribution σ_r as

$$F_z = \int_{\text{surface}} \frac{\epsilon_1}{\epsilon_0} \sigma_r E_z dS \quad (37)$$

where the z-component of the electric field (E_z) is obtained from the axial derivative of the potential function. For particles of radius $r \ll \sqrt{b^2 + z^2}$, the series expression of the z-directed force component can acceptably be truncated and normalized by r^5 to become

$$\frac{F_z}{r^5} \cong -\frac{3Q^2}{\pi\epsilon_1} \text{Re}[K_n] \frac{(z/b)}{b^7 (1+(z/b)^2)^6} = -\frac{3Q^2}{\pi\epsilon_1} \text{Re}[K_n] G_{QUAD}(z) \quad (38)$$

where $G_{QUAD}(z)$ collects the geometric dependencies, $n=2$ and

$$K_n = \frac{n(2n+1)(\epsilon_p^* - \epsilon_m^*)}{n\epsilon_p^* + (n+1)\epsilon_m^*} \quad (39)$$

Contrasting the quadrupole levitation force on a sphere in (38) with the dipolar dielectrophoretic force on a sphere in (24), two fundamental differences are evident. First, the ‘radius cubed’ dependence in the dipolar force expression is replaced by the ‘radius to the fifth’ dependence in the quadrupole case. Second, the Clausius-Mosotti factor present in the dipole expression is replaced in the quadrupole expression by the higher order K_2 term. The quadrupolar force’s dependency on (particle radius)⁵ is the distinguishing feature which makes the quadrupole an attractive component for inclusion in particle processing systems.

Isomotive Theory

Isomotive dielectrophoresis, as the name implies, is concerned with the generation of electric field topographies which exert a constant force on a particle independent of the particle’s position within the structure. Revisiting the dipolar force equation (24) and the quadrupolar force equation (38), both contain dependencies on the vertical position of the particle via the the $G_{\alpha}(z)$ and $G_{QUAD}(z)$ terms respectively. The dipole force

monotonically increases with z , while the quadrupole force increases from zero at $z=0$, followed by a maxima before decaying asymptotically to zero as $z \rightarrow \infty$. While both of these topographies are useful in particle levitation and trapping applications, of considerable utility to biological applications is the ability to separate particles of differing electrical composition. The isomotive electrode system with its position independent force characteristic offers such a capability.

The isomotive derivation begins with a solution to Laplace's equation, $|\nabla|^2 V = 0$, in cylindrical coordinates [1]

$$V = Ar^n \sin(n\theta) \quad (40)$$

for which the supporting electric field

$$E = -\nabla V = -nAr^{n-1} [\hat{a}_r \sin(n\theta) + \hat{a}_\theta \cos(n\theta)] \quad (41)$$

and

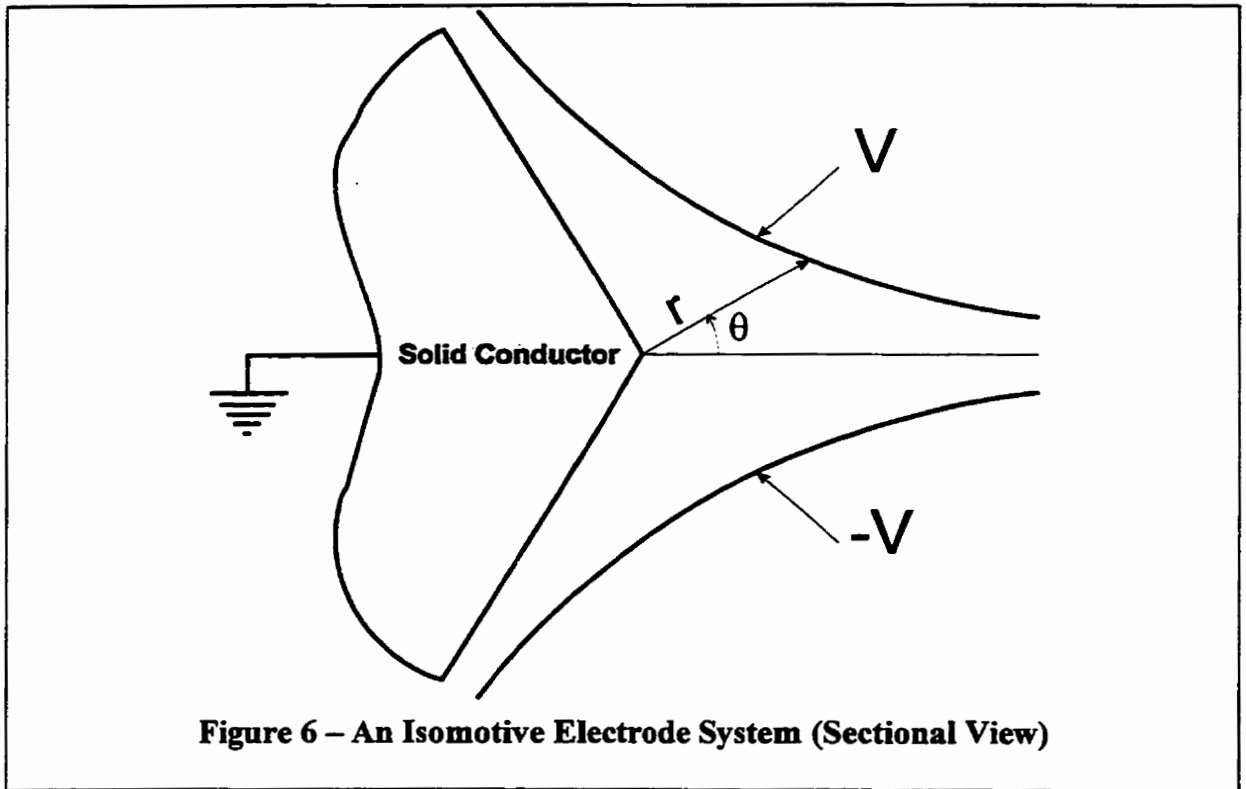
$$E^2 = E \bullet E = n^2 A^2 r^{2(n-1)} \quad (42)$$

Reusing the simple dipole force equation of (22)

$$F_e = -\frac{1}{2} \alpha v \nabla |E|^2 = -\alpha v (n-1) n^2 A^2 r^{2n-3} \hat{a}_r \quad (43)$$

To eliminate positional (r) dependence on the magnitude of this force, the condition $2n-3=0$ is imposed, thereby mandating $n=3/2$. The force in (43) now set to a constant vector, of magnitude F_{ISOM} , along the radius (r) allows for the definition

$$A = \frac{2}{3} \sqrt{\frac{2F_{ISOM}}{v\alpha}} \quad (44)$$



glass beads introduced along the center of the isomotive structure would experience a uniform acceleration and would in time (t) travel a distance given by

$$d = \frac{1}{2}at^2 \quad (47)$$

With the acceleration independent of particle size, this distance will be uniform for the entire family of glass beads. The isomotive electrode system would not assist an individual needing to sort (by size) a uniform material particle population, but an isomotive processor for segregating particles by electrical composition would be a valuable analytical tool in a variety of applications.

ELECTROSTATIC SIMULATION

Electrostatic field simulation encompasses the computer aided engineering task of numerically solving Maxwell's equations for arbitrary geometric problems. Electromagnetic simulators have gained acceptance for their ability to solve problems too complex for analytical representation. Several different numerical methods form the computational engines of various commercial solvers. While numerical comparison between different algorithms will not be provided, fundamental algorithmic differences among three popular methods (finite difference, finite element and boundary element) will be presented. For numerical simulation in this thesis, only a boundary element method software package was utilized. The simulation program is a 3-D electrostatic design package entitled Coulomb; it is one of a set of boundary element method simulation packages offered by Integrated Engineering Software of Winnipeg, MB, Canada.

Finite Difference Method

The simplest, and typically therefore the least accurate, numerical method available for electrostatic modeling is the finite difference method. A domain-type solver (involving a direct solution of the governing differential potential equation), the finite difference method is typically an iterative process whereby a truncated Taylor series expansion of the differential operator is applied at each point of a rectilinear grid over the problem region. The uniform grid used to discretize the problem space makes for crude geometric modeling particularly in regions containing highly non-linear field topographies. In open field problems (or unbounded problems), the method involves a

large number of unknowns, and consequent lengthy solution times, as the uniform grid must extend across expansive regions.

Finite Element Method

Another domain-type approach, the finite element method also solves Maxwell's equations in differential form. The problem geometry is entered, and the solution space is discretized into triangular (for 2-D FEM) or tetrahedral (for 3-D FEM) finite elements. From this discretized interpretation of the problem, a linear system of equations is compiled to calculate the electrostatic field values at the nodes of each element. Iteration to a final solution is achieved by the algorithmic goal of minimizing a function proportional to the energy of the system. The result produced by a finite element solver is the direct solution of the governing differential equation for the potential.

For bounded geometry problems (the electric field in the core of a solenoid), the generation of finite elements is less problematic than for open geometries (the electric field everywhere external to a solenoid). In the latter case, artificial boundaries must be imposed on the geometry to allow the finite element mesh to terminate. This truncation of the problem space, a field of research in itself, must be carefully performed to minimize errors in the final solution.

The discretization of space, or meshing, for finite element analysis is time consuming, but it is a critically important step. In 2-D finite element analysis, mesh generation may be done manually with the aid of a graphical interface, but automatic mesh generators are commonly provided with 2-D FEM tools. For 3-D FEM solvers, problems with providing effective representation of a 3D mesh on a 2D computer screen makes automatic 3D meshing a virtual necessity. By binding all the objects in the

problem together via the rigid mesh, the finite element method may be heavily burdened with parametric analysis of different geometries. This is because re-meshing may need to be redone prior to each solver cycle.

For many applications, shortcomings of the finite element method include:

- large problem sizes
- derivative discontinuities in the geometric model
- localized errors in fields calculated by differentiation and interpolation
- algorithmic difficulties associated with error checking
- the need to artificially truncate unbounded problems.

This is not to say that the finite element method is flawed, or flatly inferior to other methods. The method is relatively simple to implement in software, and given an appropriate mesh design, will yield precise solutions.

Boundary Element Method

The boundary element method is a boundary-type solver that has historically been ignored in favor of finite difference and finite element domain-type solvers. This is due, in large part, to the simplicity of implementing domain-type solvers in software. The boundary element method, utilizing complex integration techniques, is a complicated algorithm to program into software, whereas domain-type solvers rely on simple linear algebra to arrive at their solutions. It has not been the theory of boundary element analysis impeding its commercialization, but rather the translation of its theoretical complexity into usable software.

The boundary element method, as with any numerical method, must also discretize the problem space into elemental units, but boundary-type and domain-type solvers are

distinguished by the architecture of their elements and the form of Maxwell's equations those elements are used to solve for. The boundary element method only discretizes the boundaries between neighboring media and then solves Maxwell's equations in integral form along those boundaries. The unknowns being solved for are physical charges and currents adequate to maintain all boundary conditions prescribed by the geometry. The equivalent sources solved for in boundary element analysis, due to their physical significance, provide intuitively simple means for direct computation of global quantities such as force, torque, stored energy and capacitance. Additionally, scalar and vector field solutions emerge from integral operations which minimize errors by smoothing discretization noise in the boundary sources.

In boundary element analysis, unlike finite element analysis, unbounded problems do not require an arbitrary truncation of the problem space to be performed. Requiring elements only on the physical boundaries between media allows for real limits at infinity to remain intact. While this elemental variation delivers the benefit of a dimensional reduction in the number of elements required, some of this efficiency is lost to the increased computational complexity of the integral operation required at each element.

All things considered, researchers often find it difficult to directly compare the performance of finite element and boundary element simulation packages because their only practical similarity is that both are seeking discrete representative solutions to Maxwell's equations. The methods by which each algorithm pursues that goal are so fundamentally different that direct comparison is difficult, but it is generally recognized that specific advantages do appear for both techniques under certain circumstances.

BEM SIMULATION RESULTS

Integrated Engineering Software's 3-D electrostatic design package, Coulomb v-2.6, was used extensively to model and characterize three dielectrophoretic structures: a dipole levitator, a quadrupole levitator and an isomotive separator. A three-stage process was generally followed for each structure. Ideal geometric models were simulated and the results compared with analytical prediction. Second, information extracted from the theoretical models was used to determine voltages appropriate for biasing discrete electrodes to approximate the analog model. Lastly, the discrete electrodes were entered into Coulomb, biased with the boundary voltages obtained above and the simulations run again. This three step process forms the closed loop simulator verification method:

1. the ability of the simulator to match analytical theory is confirmed
2. optimal values for a discrete implementation are obtained from theory
3. the discrete implementation's performance is compared to theory

Dipole Levitator Simulation

In the Dipole Levitation section beginning on Page 15, the theoretical basis of a dipolar electrode architecture was presented. The traditional approach has been to machine a conducting tip into a rounded cone shape approximating one of the equipotential surfaces formed by a semi-infinite line charge over a ground plane. Experimentation based on this procedure has been used successfully to demonstrate feedback controlled levitation and to extract dielectric information from levitated particles such as plant protoplasts [16].

The attention paid here to this subject seeks to devise alternative and more readily manufacturable means for generating the axially symmetric fields required for dipole levitation. The analysis proceeds in similar fashion to that of the prior art, except that the semi-infinite line charge of Figure 4 is replaced by the finite line charge of Figure 7. The cost of this modification is that the analytical voltage expression of (33) for the semi-infinite line charge becomes much more complex in the case of the finite line charge. This in turn leads to increased complexity in the electric field (the negative gradient of the potential) and ultimately the theoretical dielectrophoretic force term containing $\nabla|E|^2$.

Utilizing the method of images, the scalar potential function to the geometry in Figure 7 can be expressed as the integral sum

$$V = \int_h^d \frac{\lambda d\xi}{4\pi\epsilon_m \sqrt{(z-\xi)^2 + \rho^2}} - \int_{-d}^{-h} \frac{\lambda d\xi}{4\pi\epsilon_m \sqrt{(z+\xi)^2 + \rho^2}} \quad (48)$$

Evaluation of this integral yields

$$V = \frac{\lambda}{4\pi\epsilon_m} \ln \left[\frac{\left(d-z + \sqrt{(d-z)^2 + \rho^2} \right) \left(h+z + \sqrt{(h+z)^2 + \rho^2} \right)}{\left(h-z + \sqrt{(h-z)^2 + \rho^2} \right) \left(d+z + \sqrt{(d+z)^2 + \rho^2} \right)} \right] \quad (49)$$

which simplifies to that for the semi-infinite line charge (33) when the limit as $d \rightarrow \infty$ is taken.

Continuing with the voltage expression from (49), and restricting the problem to the cylindrical axis, i.e. $\rho = 0$, the z-component of the electric field (E_z) is determined to be

$$E_z = -\frac{\partial}{\partial z} (V|_{\rho=0}) = -\frac{\lambda}{2\pi\epsilon_m} \left[\frac{(hd^2 - dh^2) + (d-h)z^2}{z^4 - (h^2 + d^2)z^2 + d^2h^2} \right] \quad (50)$$

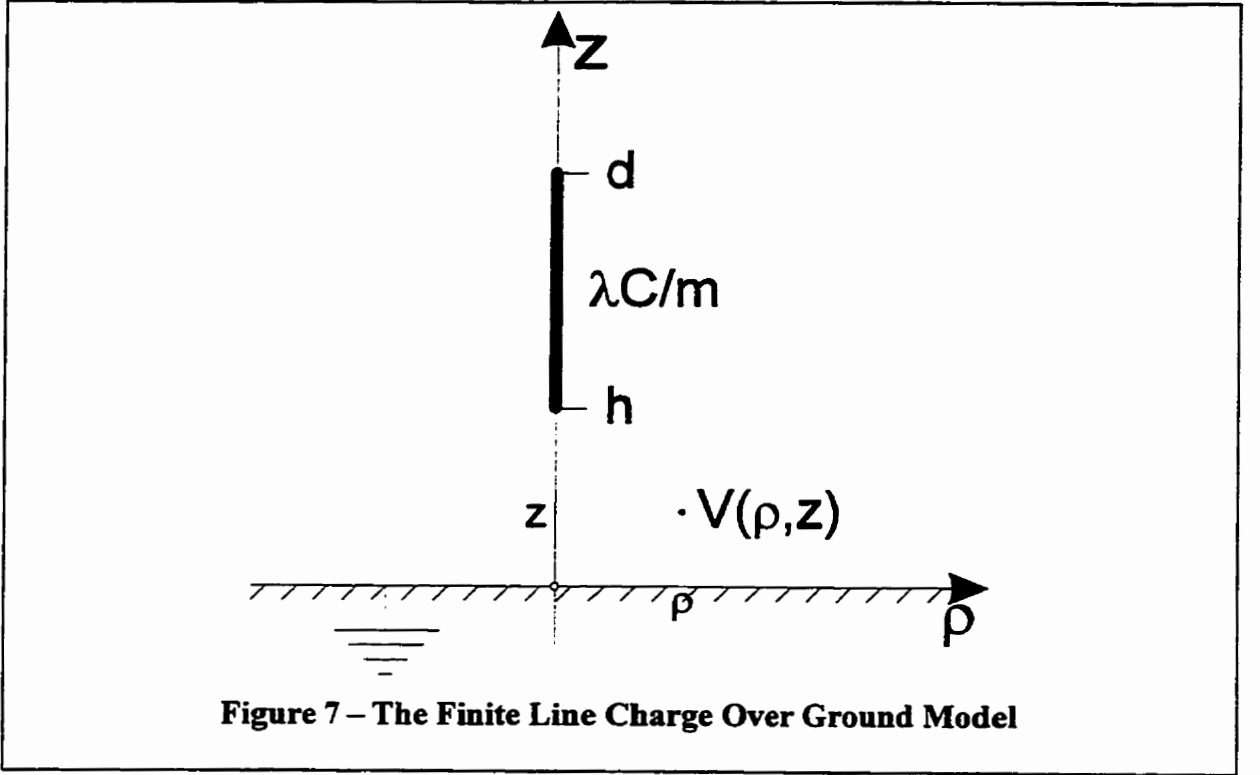


Figure 7 – The Finite Line Charge Over Ground Model

Defining for convenience

$$\begin{aligned}
 \alpha_1 &= hd^2 - dh^2 \\
 \alpha_2 &= d - h \\
 \alpha_3 &= h^2 + d^2 \\
 \alpha_4 &= d^2 h^2
 \end{aligned} \tag{51}$$

careful differentiation yields the z -axis gradient of the square of the electric field as

$$\begin{aligned}
 \frac{\partial}{\partial z} E_z^2 &= \frac{\lambda^2}{2\pi^2 \epsilon_m^2} \left[\frac{\alpha_1 + \alpha_2 z^2}{z^4 - \alpha_3 z^2 + \alpha_4} \right] \left[\frac{2\alpha_2 z}{z^4 - \alpha_3 z^2 + \alpha_4} - \frac{(\alpha_1 + \alpha_2 z^2)(4z^3 - 2\alpha_3 z)}{(z^4 - \alpha_3 z^2 + \alpha_4)^2} \right] \\
 &= \frac{\lambda^2}{2\pi^2 \epsilon_m^2} G_{Finite}(z)
 \end{aligned} \tag{52}$$

where $G_{Finite}(z)$ collects the geometric dependencies as has been done before.

Substitution of this result into (24) and normalizing to r^3 yields the theoretical

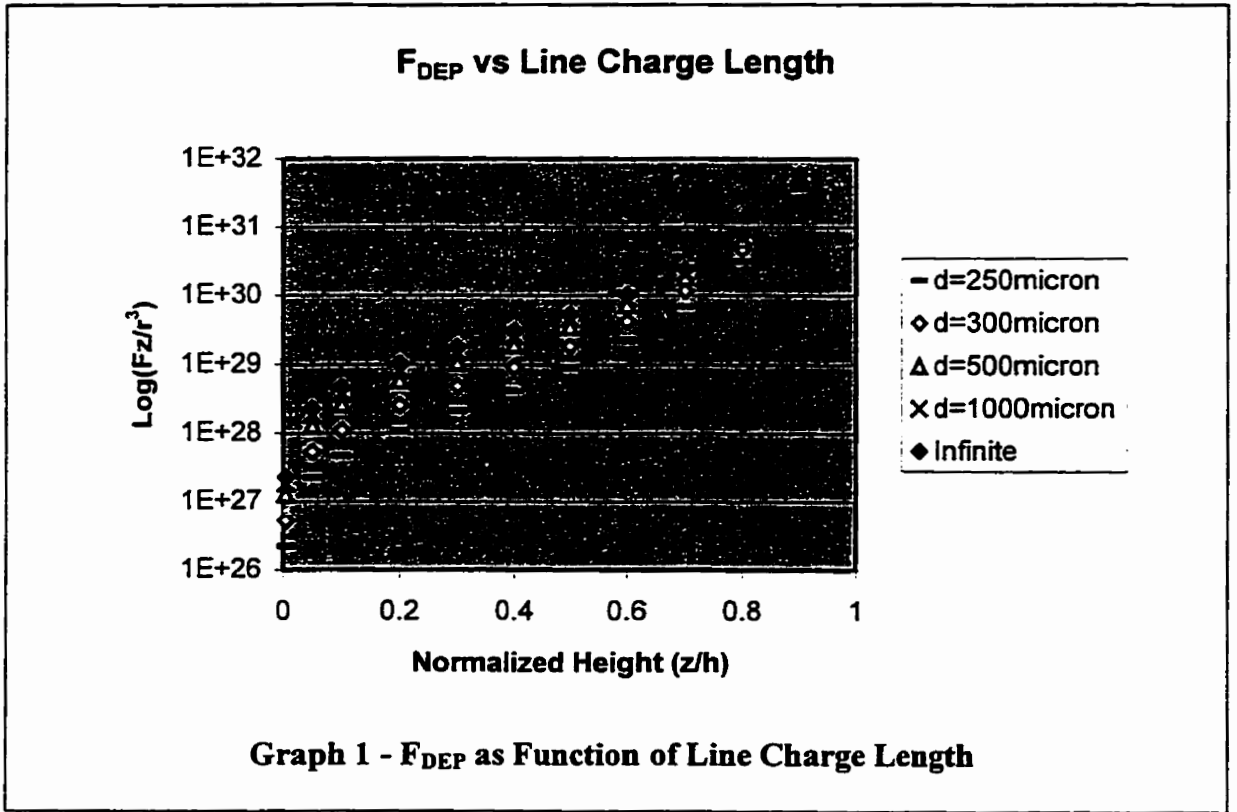
dielectrophoretic force for a homogeneous sphere centered at height z on the vertical axis in Figure 7:

$$\frac{F_{DEP}}{r^3} = \frac{\lambda^2}{\pi\epsilon_m} \text{Re}[K_1] G_{Finite}(z) \quad (53)$$

The result of (53) for a finite line charge over a ground plane takes the same form as that for the semi-infinite line charge over a ground plane presented in (36). The two expressions differ only in the geometric terms $G_{Finite}(z)$ (for the finite line charge) and $G_{\infty}(z)$ (for the semi-infinite line charge). Graph 1 shows how increasing d in Figure 7 causes the dielectrophoretic force due to a finite line charge (53) to approach that of a semi-infinite line charge (36), as must be the case in the limit.

Before relying on Coulomb to model the dielectrophoretic response of arbitrary discrete planar electrode geometries, the program's ability to correctly model analytically manageable dielectrophoretic phenomenon was to be confirmed. The first such simulation studied the dielectrophoretic levitation force profile on a homogeneous sphere subject to the electric field of a finite-line charge over a ground plane (Figure 7).

Initially anticipated to be a relatively simple exercise, this 'simulator verification' phase of the work was made dramatically more difficult by Coulomb's inability to correctly calculate the body force on a neutral object in a non-uniform electric field; the fundamental precept of dielectrophoresis. A simulation was prepared demonstrating Coulomb's violation of fundamental energy principles, and this was used by IES to debug the software package and produce an updated version.

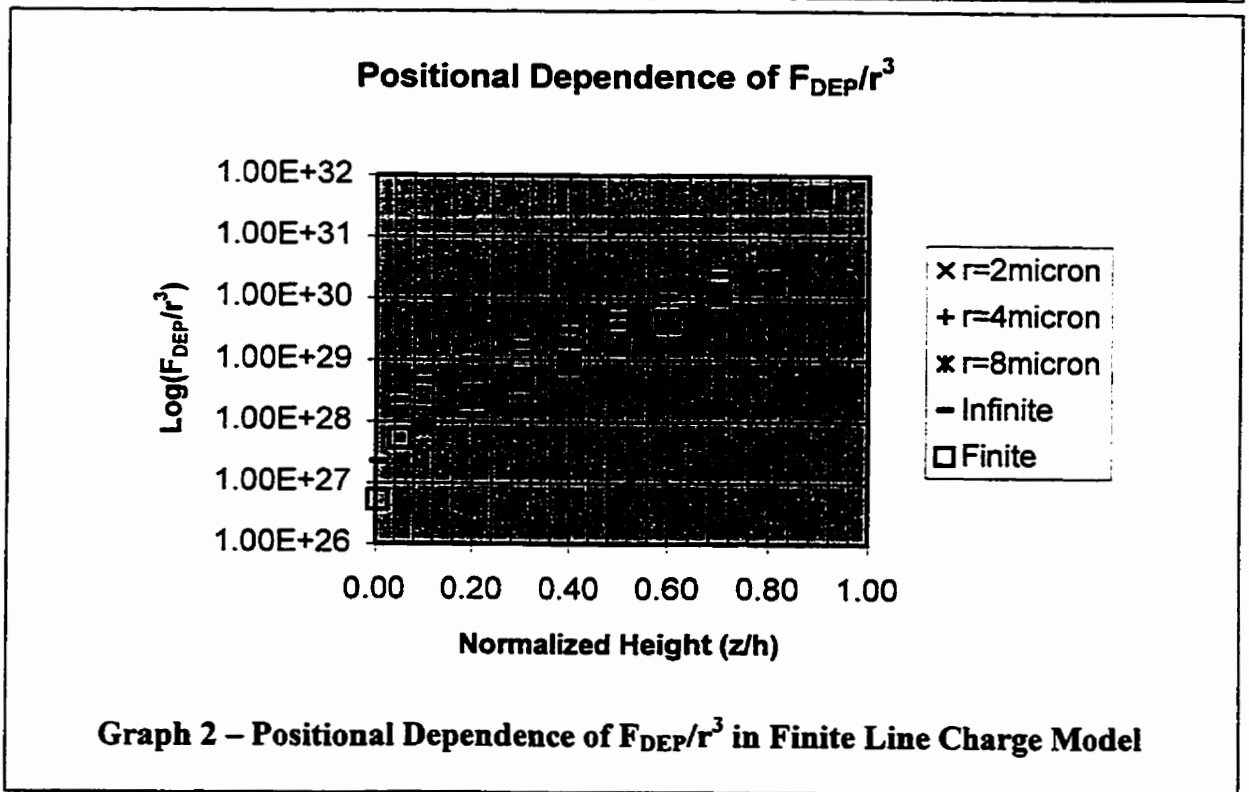
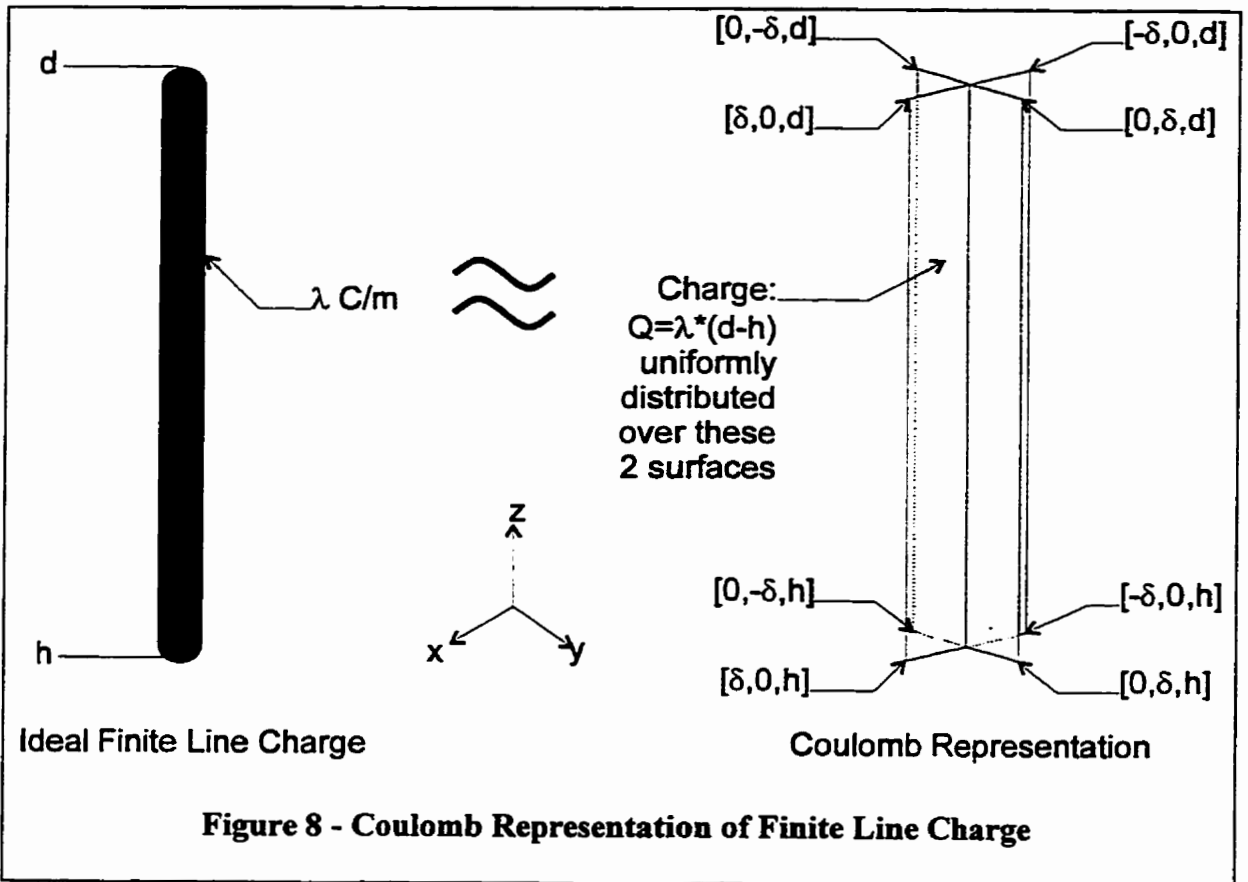


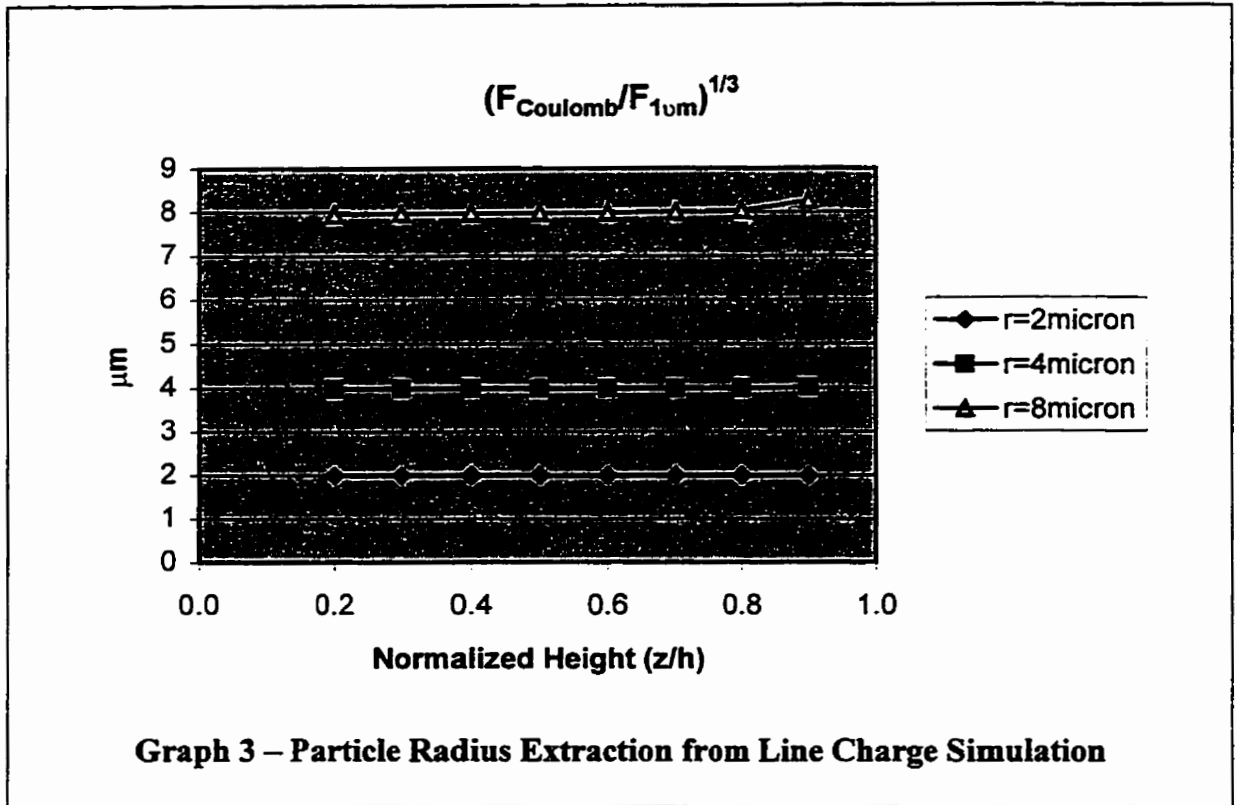
To study the finite-line charge dielectrophoretic force profile, the ‘universe’ in Coulomb was taken to be free-space, test particles were assigned a relative permittivity $\epsilon_p=4.0$ and the solver was run in DC-permittivity mode. The analysis therefore neglects particle and media conductivities (taken to be zero) and reduces the Claussius-Mosotti polarization factor (23) to a real number.

For the dipole levitation simulations, a finite line-charge model was used in place of the analytically simpler semi-infinite model. This was required because Coulomb does not support objects infinite in extent. Additionally, Coulomb does not support true ‘line-charges’, so the finite line charge was represented as two orthogonal rectangles defined by $[(\delta, 0, h), (-\delta, 0, h), (-\delta, 0, d), (\delta, 0, d)]$ and $[(0, \delta, h), (0, -\delta, h), (0, -\delta, d), (0, \delta, d)]$ as illustrated in Figure 8. These parameters were chosen to be $h=200\mu\text{m}$, $d=300\mu\text{m}$ and

$\delta=1\mu\text{m}$. A total charge of 1 Coulomb was distributed over these two surfaces to approximate a $100\mu\text{m}$ line-charge with charge per unit length $\lambda=1.00\text{E}+04\text{C/m}$. To eliminate the need to geometrically define and element either a ‘truncated infinite ground plane’ or an ‘image line-charge’, anti-symmetry about the $z=0$ plane was defined in Coulomb. This condition mirrors all geometry across the plane of symmetry and negates boundary conditions on the mirrored geometry, i.e. an image line-charge approximation carrying a total charge of -1C extends from $z=-h$ to $z=-d$. The values h , d and λ define the physical parameters required for analytical tabulation of the normalized dielectrophoretic forces (equations (36) and (53)) on particles centered at various axial heights z .

An individual simulation run comprised the introduction to the line-charge model of a dielectric sphere of radius r , centered at a height z and filled with a dielectric material of relative permittivity 4. To confirm that both the z -position and radial dependencies on the dielectrophoretic force are modeled correctly by Coulomb, a batch analysis was run whereby three particles of radii $2\mu\text{m}$, $4\mu\text{m}$ and $8\mu\text{m}$ were translated from $z=40\mu\text{m}$ to $z=180\mu\text{m}$ in $20\mu\text{m}$ increments. At each vertical position, for each particle, the net body force (in Newtons) acting on the particle was numerically solved for. The force values obtained were normalized by $1/r^3$ and compared with the analytical prediction (53).





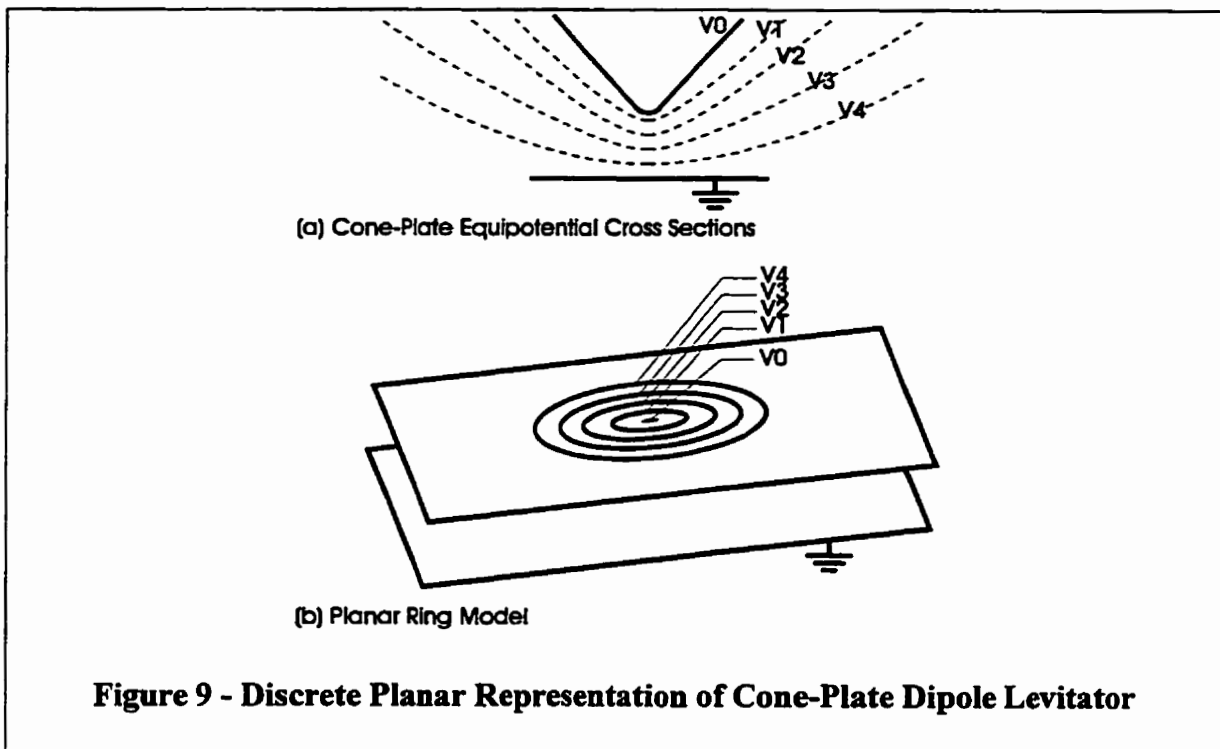
The results of the above analysis are depicted in Graph 2 and Graph 3. Graph 2 is a log axis plot of the radially normalized dielectrophoretic force. Shown in the plot are normalized results from Coulomb for the 2 μm , 4 μm and 8 μm particles, the analytical force profile for the finite-line charge model and the analytical force profile for the semi-infinite line charge model (for reference). As can be seen, the agreement between the finite model's analytical profile and the results obtained numerically from Coulomb are good.

Graph 3 depicts an alternate analysis of the data whereby the force data from Coulomb is transformed by first dividing by the radially normalized analytical value and then taking the cube root of the result. This transformation should yield the radius (in microns) of the test particle, and should therefore be constant for each particle at each z-

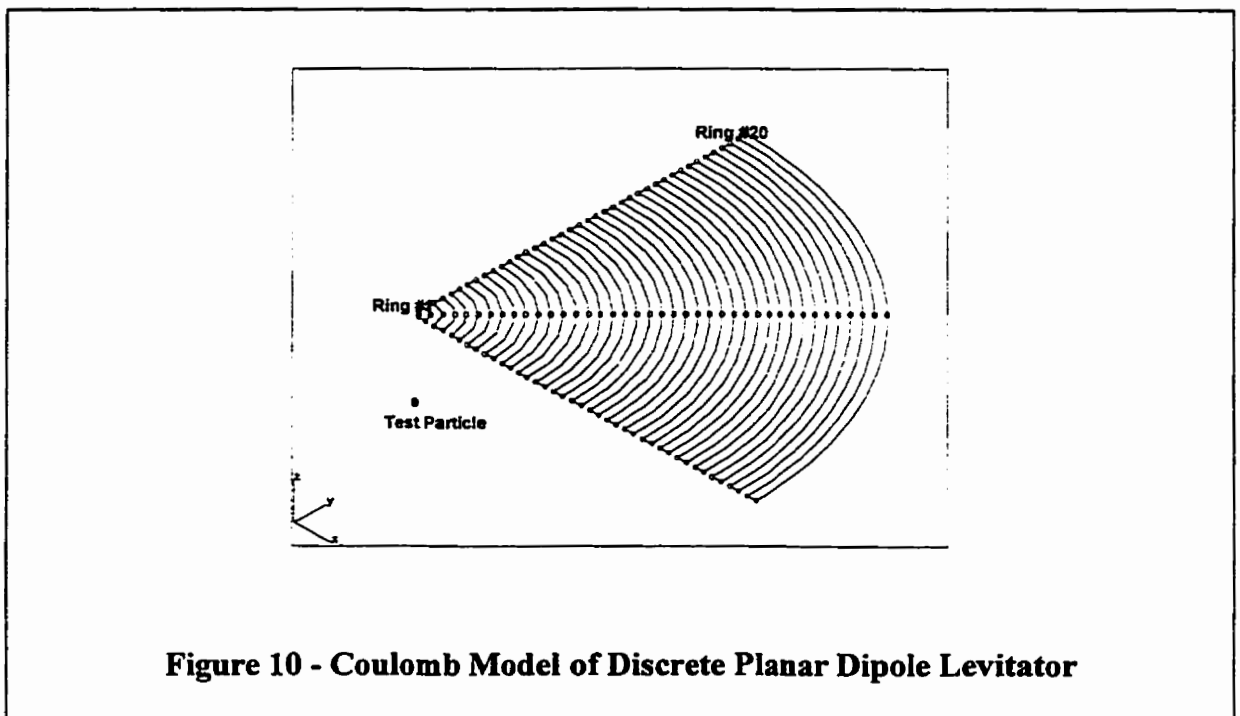
position. Graph 3 displays the results of this analysis and confirms the validity of the Coulomb solutions.

Having confirmed Coulomb's ability to model the dipolar dielectrophoretic force response for the finite line charge over a ground plane, a discrete planar electrode geometry capable of emulating the dipolar levitation profile configuration is sought. Figure 9 depicts the concept behind the discrete planar dipole levitator geometry. Using the analytical solution for the voltage (33) due to a semi-infinite line charge with $\lambda = 1.25 \times 10^{-9} \text{ C/m}$ at a height $h = 510 \mu\text{m}$ over a ground plane in free space, the potential was computed at 20 points defined by

$$[\rho, z] = [50 \mu\text{m} + n * 100 \mu\text{m}, 500 \mu\text{m}] \text{ for } n = 0..19 \quad (54)$$



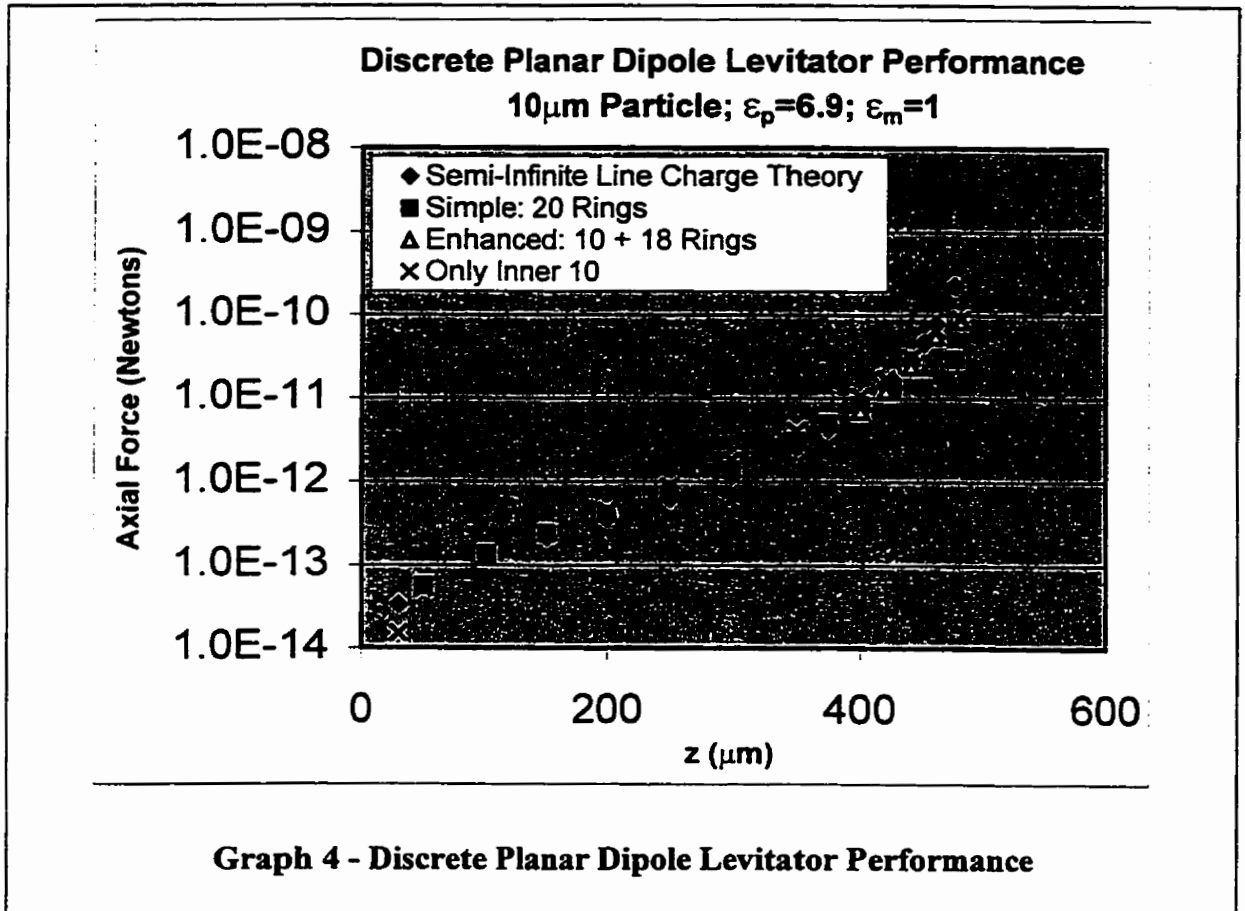
Geometry consisting of twenty quarter circles centered at $[0,0,500\mu\text{m}]$ with radii matching the ρ co-ordinates set out in (54) were entered into Coulomb. The thickness, or line-width, of each of these quarter circles were $50\mu\text{m}$. The circles were confined to the quadrant defined by $(x > 0, y > 0)$. Voltage boundary conditions were assigned to each of the quarter circles such that the boundary voltage on a particular arc was the voltage



predicted by theory at the center of that node's $50\mu\text{m}$ width. Symmetry was then defined about the $x=0$ and $y=0$ planes, while anti-symmetry was defined about the $z=0$ plane. Under these conditions, the overall system effectively becomes twenty concentric rings centered at $[0,0,500\mu\text{m}]$ carrying positive voltage boundary conditions and a set of

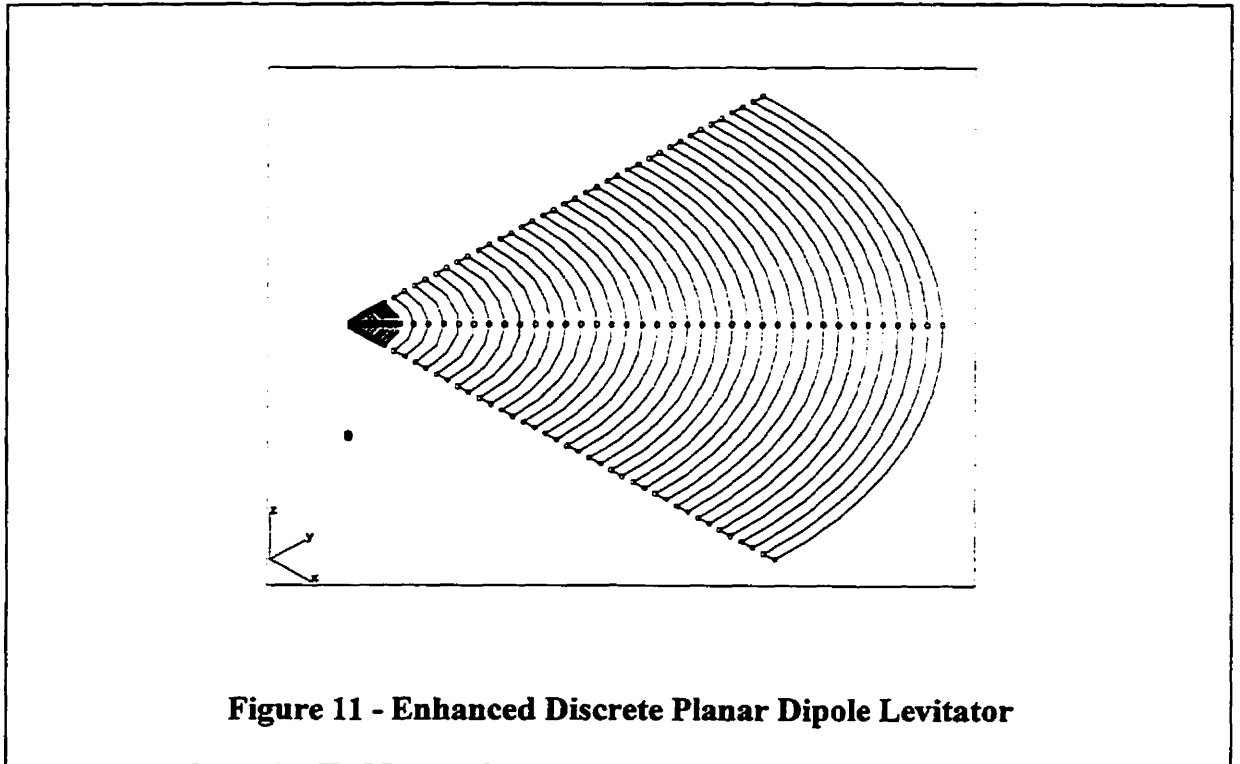
twenty image rings located at $z=-500\mu\text{m}$ carrying the opposite voltage boundary conditions.

To test this structure's ability to emulate the dielectrophoretic force profile of the



semi-infinite analytical model, a test particle was introduced into the geometry. A 10 μm radius spherical test particle with relative permittivity 6.9 is centered along the z -axis and translated from a center height of 30 μm up to 480 μm . At each height, the solver was run and the net body force acting on the sphere was computed. It should be noted that with the symmetry conditions defined, the spherical particle was represented in the geometry

as only the portion of the total sphere residing in the quadrant ($x>0,y>0$). Consequently, to get the representative force on the total sphere, the drawn $\frac{1}{4}$ sphere was selected and Coulomb was instructed to also include the three image segments located around the z-



axis in the force calculation. The negative image sphere existing below $z=0$ was not included as, by symmetry, the *net force* on the upper sphere *and* its image would be zero. The total geometry drawn in Coulomb is illustrated in Figure 10 where the twenty concentric $\frac{1}{4}$ rings are visible converging above the $\frac{1}{4}$ spherical test particle.

In Graph 4, the results of this parametric analysis are presented whereby the performance of the discrete planar electrode configuration generally agrees well with the analytical model from which it was derived. However, the deviation between the two devices does become extreme in the region approaching the surface of the planar

electrodes. As this is presumably the region where feedback assisted levitation may be performed, this defect is of concern and needs to be addressed. A modified simulation was run whereby the inner two rings were replaced by 10 rings of $8\mu\text{m}$ line width spaced $17.5\mu\text{m}$ apart (center-to-center) as shown in Figure 11. This data, also portrayed in Graph 4, shows the effect on the force profile over the region of interest to now be compliant with the theoretical prediction. Lastly, a simulation was run with all of the periphery rings removed and only the dense inner ten rings added in the previous simulation. The data indicates that this too approximates the analytical model relatively well, but additional work would need to be performed to further characterize these structures for additional factors affecting levitation; e.g. radial stability.

Quadrupole Simulation

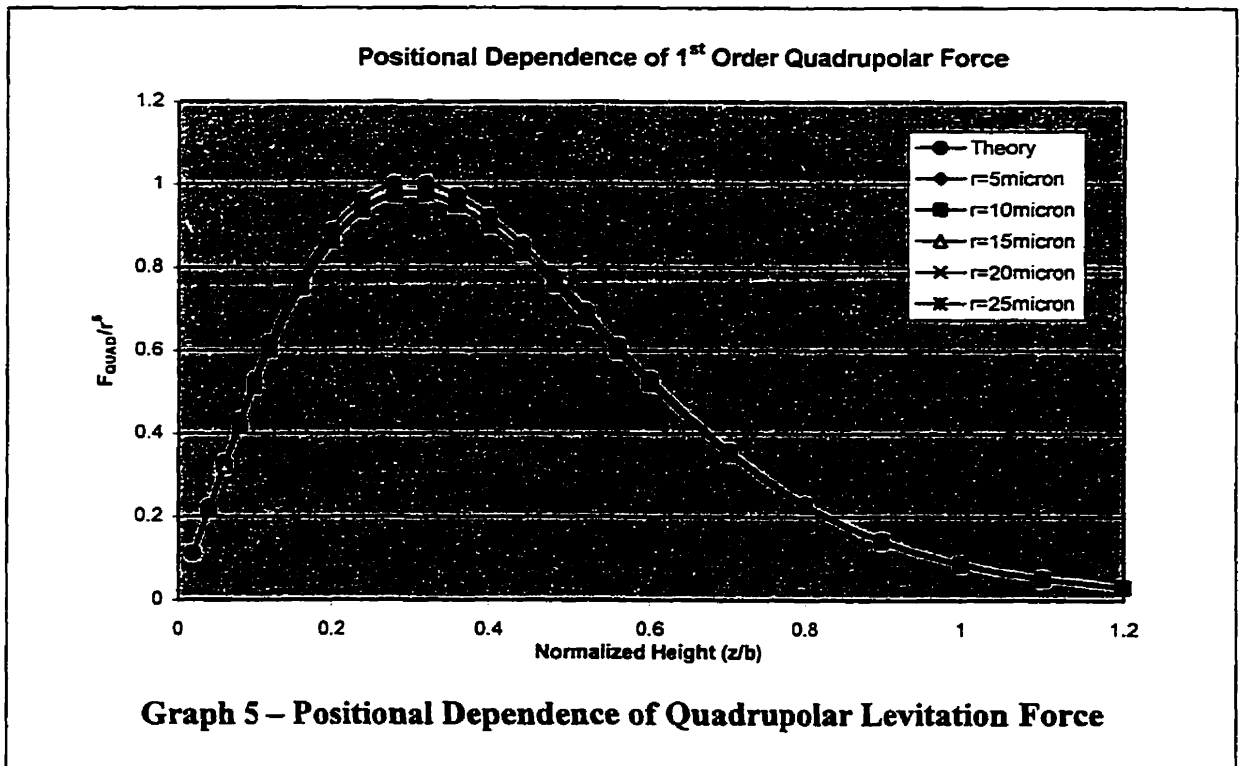
While mechanistically more complex than dipolar dielectrophoresis, multipolar dielectrophoresis has been rigorously examined theoretically [2,3,13] and some experimental verifications have been undertaken [10]. As a diagnostic tool, quadrupole levitation offers researchers insight into the detailed electrical composition of materials. A test particle trapped in the quadrupole field may be passively levitated at a height determined by the electrical properties of the media and the particle, particle geometry and non-linearities of the applied electric field.

To address the issue of quadrupole simulation, an approach similar to that used for the dipole levitator simulation was adopted. In the case of the quadrupole however, a

more precise representation of the analytical structure is possible in Coulomb, four spheres of radius $0.5\mu\text{m}$ were placed at

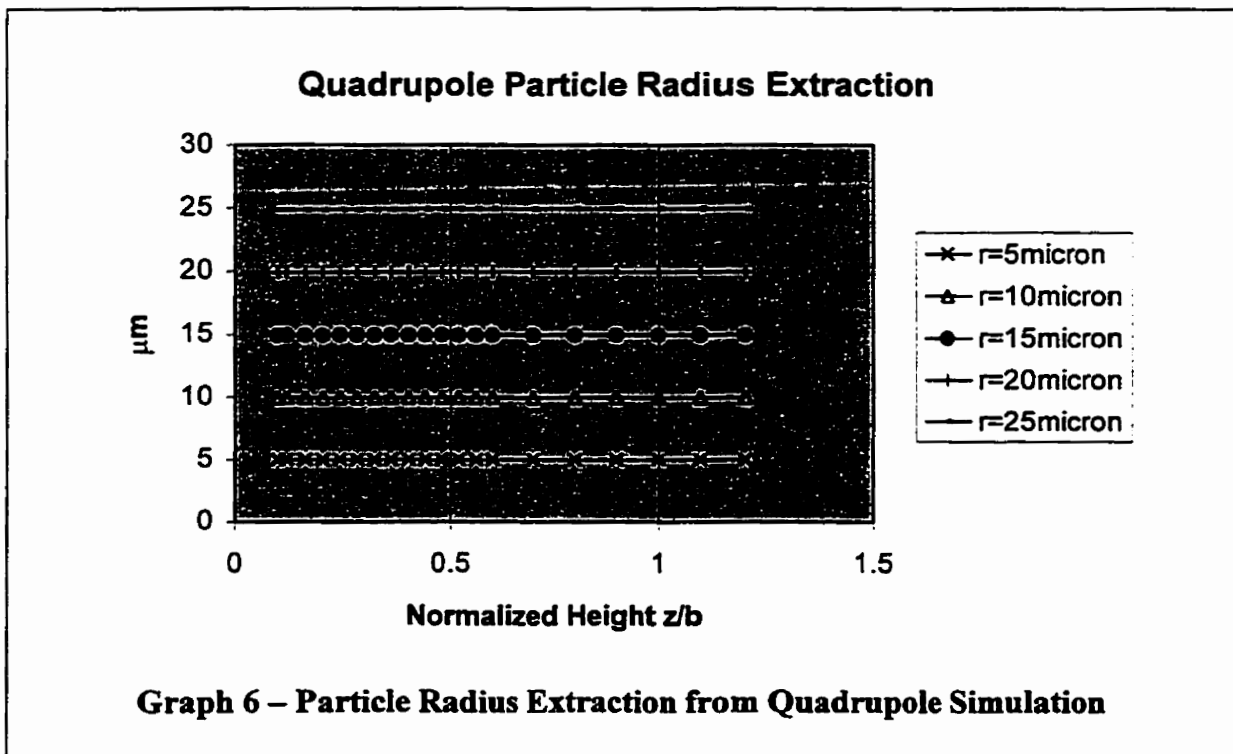
$$[(250\mu\text{m},0,0), (0,250\mu\text{m},0), (-250\mu\text{m},0,0), (0,-250\mu\text{m},0)]$$

in a 'universe' filled with water of permittivity 80; this geometry is that illustrated in Figure 5 on page 17 with $b=250\mu\text{m}$. The spheres located on the x-axis each had imposed a total charge of -1C distributed uniformly over their surfaces. Conversely, the two spheres located on the y-axis each received a total charge of $+1\text{C}$ uniformly distributed over their surfaces. Five test particles of relative permittivity 4 and radii $5\mu\text{m}$, $10\mu\text{m}$, $15\mu\text{m}$, $20\mu\text{m}$ and $25\mu\text{m}$ were individually positioned in the structure along the z-axis at heights ranging from: $5\text{-}30\mu\text{m}$ in $5\mu\text{m}$ increments and $30\text{-}300\mu\text{m}$ in $10\mu\text{m}$ increments.



As with the dipole simulation, Coulomb was run in DC-permittivity mode to eliminate conductivity and reduce the polarization factor (K_2) to a real number. The net body force acting on the test particle was computed for each z -location.

Analysis of the results from this parametric run first set out to verify Coulomb's ability to demonstrate the r^5 dependence predicted by the multipolar moment method in (38). Force data produced by Coulomb was transformed by $1/r^5$, normalized to the peak analytical force and plotted in Graph 5 against the z -height normalized by the parameter b . Coulomb's force data clearly confirms theoretical predictions. Both multipolar moment quadrupole theory and the Coulomb simulator are confirmed by these results. An alternate interpretation of the data is similar to that used in the 'finite line charge over ground' dipole force simulation; namely radius extraction. Parametric data obtained from Coulomb was first divided by the radially normalized theoretical force and the 5th root of



the result was taken. This is in contrast to the cube root operation required to perform radius extraction from dipolar dielectrophoresis data. The constancy of this transformation throughout the z-axis range, as illustrated in Graph 6, strongly supports multipolar moment quadrupole theory once again.

Isomotive Simulation

Verification of the isomotive structure by simulation proceeded slightly differently than the methods used for the cone-plate and quadrupole geometries. In the two latter cases, the existence of a free charge analog model allowed for nearly exact geometric representation in Coulomb. The isomotive electrode structure, on the other hand, stems from purely mathematical roots whereby the following condition is enforced:

$$E \cdot \nabla E = \text{Constant} \tag{55}$$

An electrostatic potential expression which satisfies the above relationship is obtained analytically and used to define equipotential surfaces capable of sustaining the isomotive relationship. This scalar potential field is infinite in extent, and no simple finite charge model exists which would allow precise representation in a bounded geometry simulator. Nevertheless, the methodology for deriving the discrete electrode geometry and the means by which it is tested are very similar to the method already performed for the ring dipole levitator. How they differ is that the simulator is not used to characterize an analytical model (because none exists), but rather the discrete isomotive structure is compared to an analytical expectation directly.

As an aside, the isomotive field structure would be more simply represented in Electro (the 2D analogue to Coulomb), but this package was not made available to our

facility. Using a 3D simulator to model a 2D problem requires an arbitrary truncation of the infinite third dimension and would be a source of edge effect errors at the peripheries of the model. As this is presumably not a region in which dielectrophoretic separation would be sought, the significance of this degradation may be minimal.

Recalling equation (45) which defines the equipotential surfaces in the isomotive structure, and considering this potential field as a 2D field, the potential at a discrete set of N points (p_n) defined by

$$p_n = (X_1 + (n-1)X_s, h) \quad (56)$$

where

$$\left. \begin{array}{l} 1 \leq n \leq N \\ X_1 \Rightarrow \text{First point} \\ X_s \Rightarrow \text{Electrode spacing} \\ h \Rightarrow \text{Vertical position.} \end{array} \right\} \quad (57)$$

The electric potential at each of these points can be obtained from (45) through the transformations

$$\begin{aligned} r_n &= \sqrt{(X_o + nX_s)^2 + h^2} \\ \theta_n &= \text{atan}\left(\frac{h}{X_o + nX_s}\right) \end{aligned} \quad (58)$$

The set of voltages $[V_n]$ may be used to emulate the isomotive field when used to bias a set of N coplanar electrodes spaced apart by X_s vertically mounted by a height $2h$ over an identical set of electrodes biased at the set of potentials $[-V_n]$.

The Coulomb geometry used to represent the discrete isomotive structure is shown in Figure 12. The designation of anti-symmetry about the $z=0$ plane simplified the geometry in that only the upper set of electrodes needed to be drawn and discretized into elements. The length of each electrode was taken to be 3mm long, and all force computations were carried out at the midline to minimize truncation edge effects. As was the case when modeling a finite line charge over a ground plane, anti-symmetry essentially defines the image conditions necessary to induce an infinite ground plane. To utilize the structure of

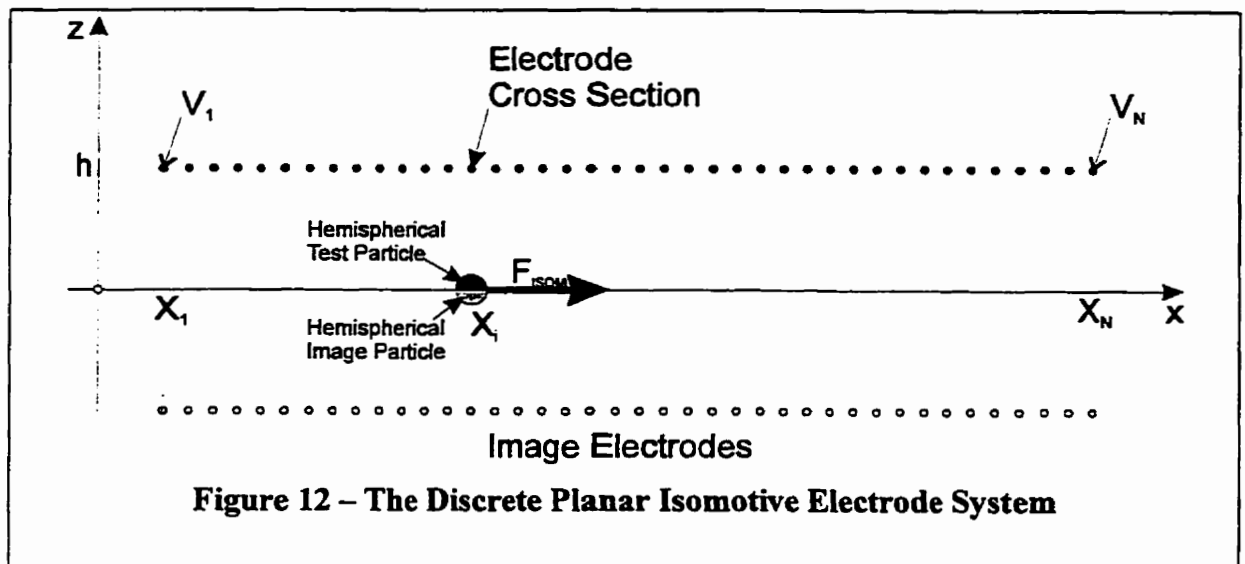
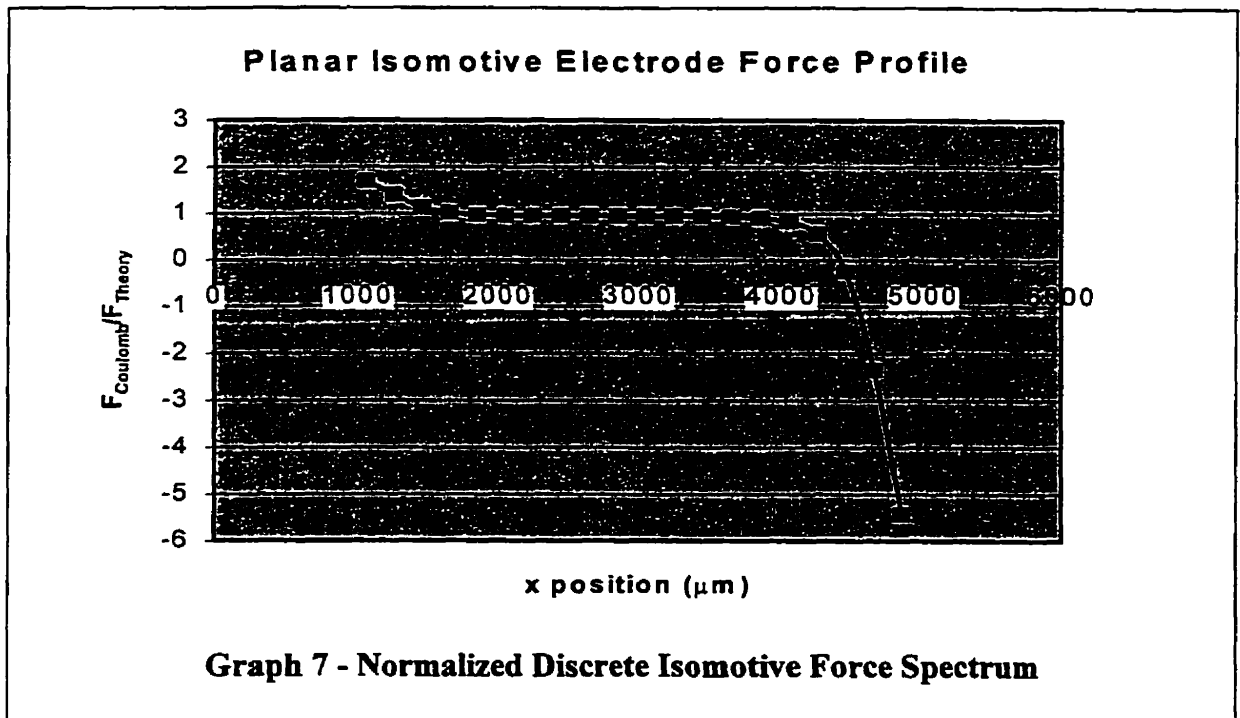


Figure 12 as an isomotive separator, the structure is mounted vertically, and a particle stream is injected into the structure from the top at point x_i in Figure 12. A polarizable particle entering the isomotive structure at this point will be forced in a direction parallel to the x -axis. To characterize this discrete isomotive model, a hemispherical particle is positioned with its circular flat flush with the $z=0$ plane as illustrated in Figure 12. The particle is parametrically translated from left to right in Figure 12. At each position, the 3D solver is run and the net force acting on the hemisphere (and its image) is computed.

This force is equivalent to the net force that would be exerted on a spherical particle centered at $(x_i, 0)$ along the midline between a pair of anti-symmetrically biased discrete electrode sets.

The results of the parametric coulomb simulation are presented in Graph 7. The vertical axis is the simulated force normalized by the expected isomotive force; F_{ISOM} in (44). An exact representation of the isomotive structure would have yielded a flat line throughout the structure at 1.0 in Graph 7. As can be seen from Graph 7, the discrete planar structure is isomotive at the prescribed force magnitude throughout the central region of the device, but isomotive behavior breaks down at the device edges where fringing fields due to truncation distort the isomotive field.



EXPERIMENTAL WORK

Experimental studies performed over the course of the project were aimed at validating multipolar moment quadrupole theory. Discrete planar quadrupole chips were fabricated, boundary element simulation was performed to model the planar devices and an opto-mechanical chamber was designed to house the quadrupole chip for cross-plane observation. To verify analytical quadrupole theory, an experimental quadrupole force profile (similar to that in Graph 5) and an experimental demonstration of radius extraction (as in Graph 6) was sought. The arrangement of the various laboratory components used during experimentation is shown in Figure 13.

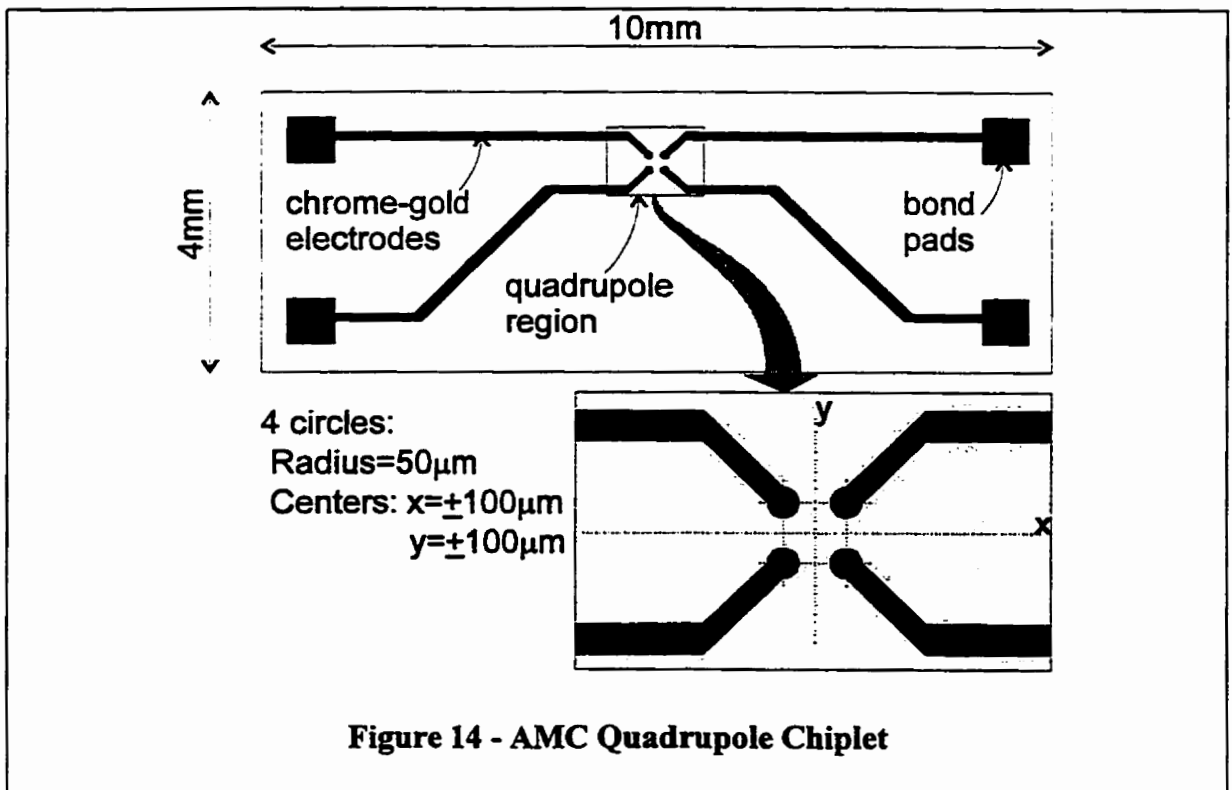
The Discrete Planar Quadrupole Device

To experimentally study multipolar moment quadrupole theory, the discrete planar



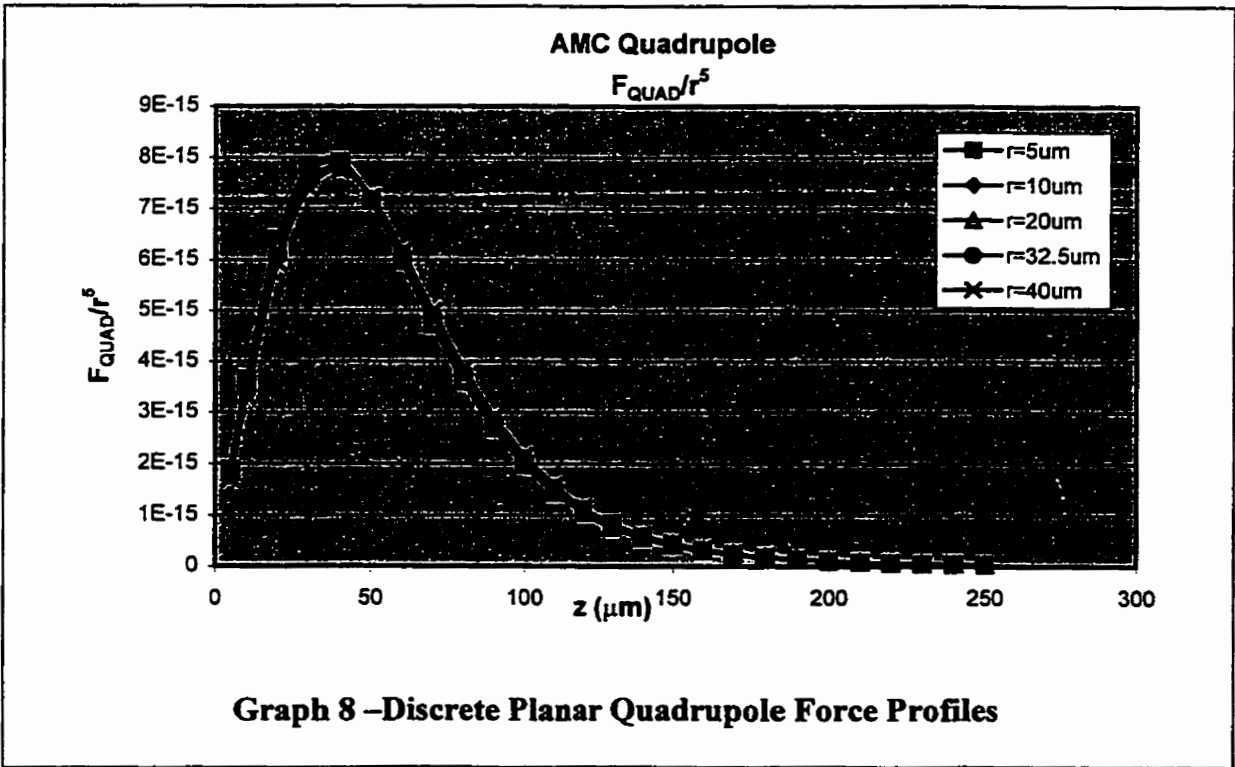
Figure 13 - Laboratory Equipment Arrangement

quadrupole device of Figure 14 was fabricated at the Alberta Microelectronics Center in Edmonton, AB. Shown in the figure are the dimensions of the quadrupole region as well as the overall chiplet size. The substrate was $500\mu\text{m}$ thick glass upon which unpassivated chrome-gold electrodes were patterned. This electrode configuration seeks to emulate the point-charge quadrupole arrangement. While an analytical solution exists for the point charge topography, physical implementation is not attainable. Two steps were required to experimentally characterize the discrete planar quadrupole. First, an analytical point-charge model capable of adequately representing the discrete planar quadrupole was sought. Secondly, an experimental force profile was gathered through levitation experiments to enable the key predictions of multipolar moment quadrupole theory to be tested.

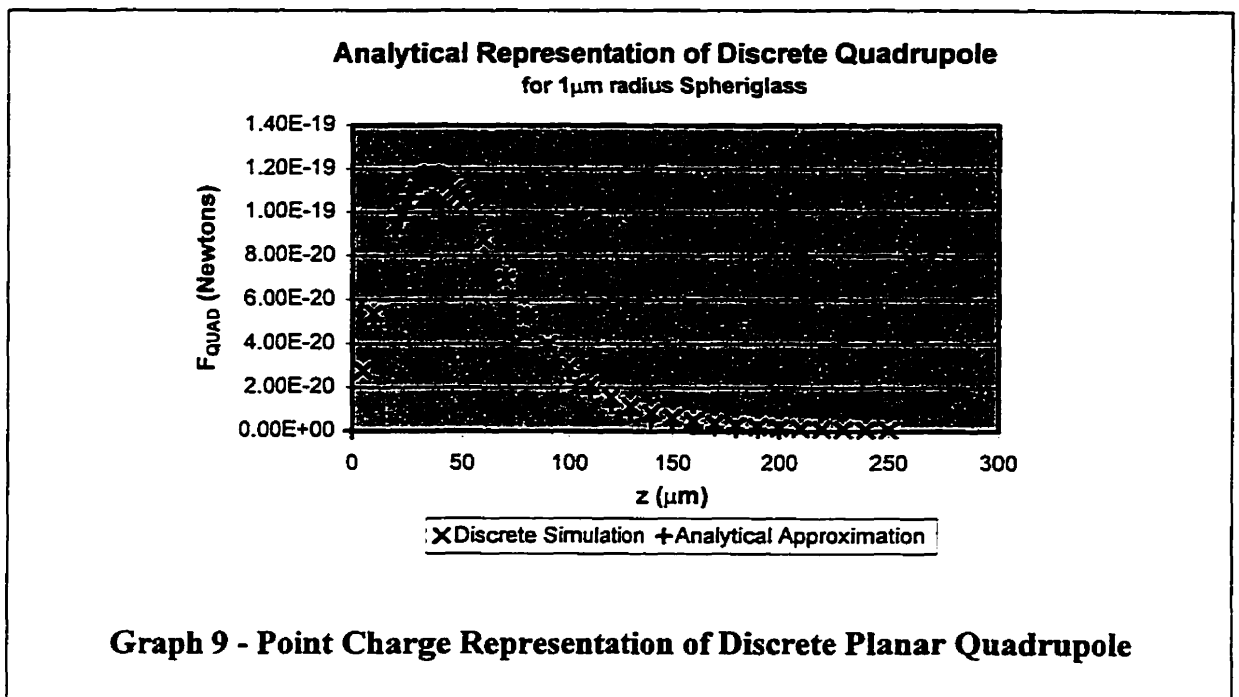


Numerical Modeling of the Planar Quadrupole Device

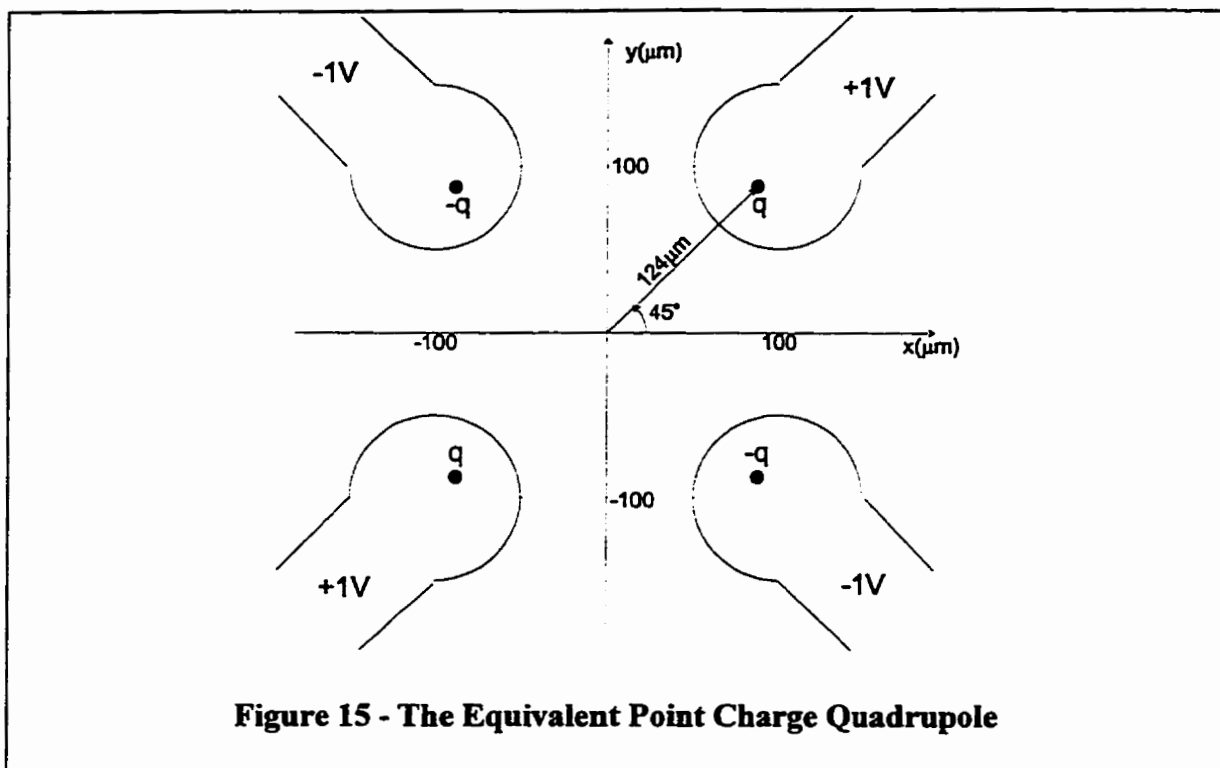
To address the degree to which the discrete planar quadrupole emulates a point-charge quadrupole, boundary element simulation was employed to determine the dielectrophoretic force on a variety of spherical objects parametrically translated through a range of heights above the center of the discrete planar quadrupole surface. From a qualitative point of view, the force profiles for the discrete planar quadrupole must mimic those of the analytical solution of Graph 5, Page 39. The results of this analysis are shown in Graph 8, and it can be seen that Coulomb does predict a similar profile. The radii of particles used in this simulation ranged from 5 μm to 40 μm and the particles were centered at vertical positions between 5 μm and 250 μm above the surface.



To this data, an equivalent point charge quadrupole was then fit with the motivation being that a simple analytical prediction of the physical device's dielectrophoretic force profile would be useful when correlating experimental data to theory. To find this optimal equivalent quadrupole, the following procedure was used. A Coulomb simulation was first run on the discrete planar electrode geometry biased at ± 1 V with a $1\ \mu\text{m}$ radius particle of permittivity 6.9 translated from $5\ \mu\text{m}$ to $250\ \mu\text{m}$ above the center of



the quadrupole region. At each height, the electrostatic solver was run and the body force on the particle was numerically computed. Optimization of the parameters b and q in the point charge quadrupole force equation (38) was now possible. Increasing b (moving the charges farther apart) has the effect on the force profile of both decreasing the peak force value and shifting its location to a higher vertical position on the z -axis. The point charge spacing (b) is adjusted to align the maxima of the equivalent analytical force profile with



that produced by Coulomb simulation. The charge magnitude (q) is then set to equate the maxima of the analytical prediction to the maximum value yielded by Coulomb.

By this method, the optimal value for b was determined to be $124\mu\text{m}$ with a q value of 2.76×10^{-13} Coulombs. The result is an equivalent point charge quadrupole that closely matches the discrete planar quadrupole's dielectrophoretic force profile at $\pm 1\text{V}$ bias. The numerically obtained Coulomb data and the analytical fit to that data are plotted together in Graph 9 to demonstrate their close agreement. Figure 15 demonstrates the physical relationship between the equivalent point charges and the discrete planar electrodes which they model. The analytical fit to boundary element simulation data now offers a reliable benchmark for the experimental data.

Discrete Planar Quadrupole Chamber Assembly

Having characterized the discrete planar electrode system through boundary element method simulation, experimental demonstration of the results was sought. To achieve this goal, a chamber able to deliver particles into a horizontally viewed active quadrupole region was needed. A horizontal viewing architecture was required to allow for precise measurement of the vertical displacement during levitation. A variety of chamber designs were built and tested for their ability to meet this surprisingly difficult specification. The fruit of this design effort was the quadrupole fluid integrated circuit chamber of Figure 16. As will be demonstrated, the final system performed very well, although areas for future improvement were identified.

Assembly of the lead carrier assembly proceeded as follows. A glass spacer (2.5mm thick) was bonded into the lead carrier's die well using Dow Corning's Silastic® brand

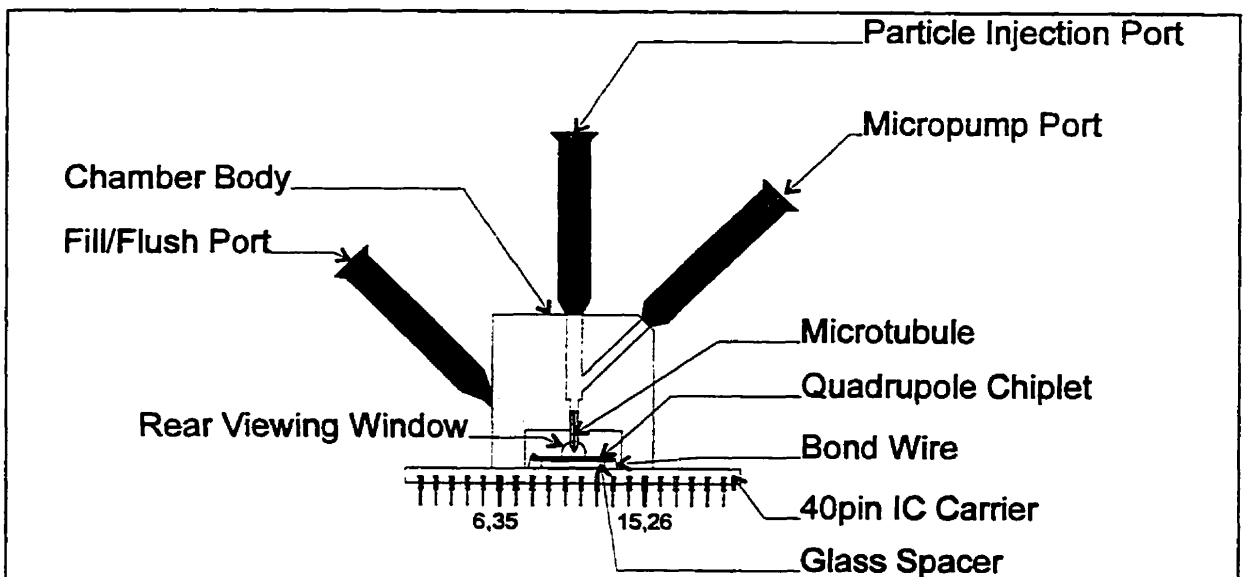


Figure 16 - Quadrupole Fluid Integrated Circuit Chamber – Front X-Section

adhesive sealant. The quadrupole chiplet (Figure 14, Page 46) was subsequently bonded on top of the spacer so that the active quadrupole region was over the center of the lead carrier's die well. Circuit Works 2400 Conductive Epoxy was used to electrically connect the four quadrupole chiplet pads to the die well's corner bond-pads (package pins 6,15,26,35).

The chamber housing itself was machined out of Lucite plastic. The horizontal viewing holes were sealed with glass coverslips epoxied onto the inner surface of the chamber cavity. The inner surface was chosen so as to prevent air bubbles from becoming trapped in the recession that would have otherwise existed. Throughout early experimentation, air bubbles in the system were identified as extremely disruptive to desired chamber operation and extensive steps were taken subsequently to prevent their formation.

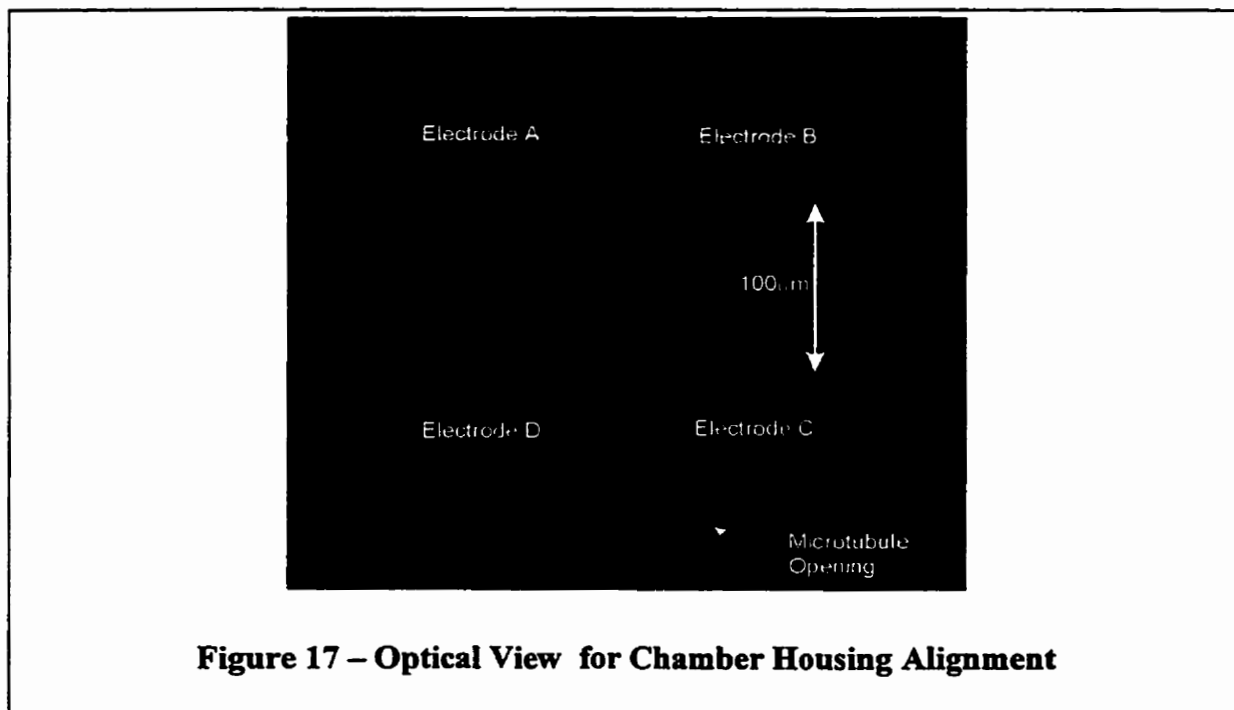


Figure 17 – Optical View for Chamber Housing Alignment

The particle injection microtubule (1mm outside diameter; $\sim 150\mu\text{m}$ inside diameter) is bonded into the vertical shaft drilled into the upper surface of the milled chamber cavity. The microtubule is recessed into the shaft deep enough to leave approximately a $500\mu\text{m}$ gap between the tapered tip of the microtubule and the surface of the quadrupole chiplet. The proximity of the microtubule's tip to the quadrupole substrate was necessary for hydrodynamic particle manipulation via the quadrupole fluid circuit.

Having now separately assembled these two pieces, the chamber housing needed to be precisely positioned over the $100\mu\text{m}$ central quadrupole region and bonded into place. To achieve this, the lead carrier assembly was inserted into a socket mounted on a standard microelectronics probe station. Silastic[®] sealant was applied to the bottom surface of the chamber housing and the housing was then placed over the lead carrier so the quadrupole chiplet recessed freely into the chamber cavity. A tight seal would be formed around the perimeter of the die-well once the sealant had been allowed to cure. Prior to the adhesive fully curing, the probe station's vertically oriented optics are used to locate, through the $150\mu\text{m}$ microtubule opening, the center of the discrete planar quadrupole region. The housing is carefully adjusted until the tips of the four quadrupole electrodes are each visible through the opening in the microtubule. At this point the particle injection microtubule is centered directly above the active quadrupole region. The adhesive used allows for a few minutes of chamber mobility while the quadrupole region is located (optically) and the chamber housing is adjusted (by hand). A snapshot taken through the probe station optics during chamber system assembly is shown in Figure 17 in which the tips of the 4 gold electrodes can be seen in the central region.

Once the adhesive has been allowed to fully cure, 4mm long 16 guage needles were epoxied into the chamber's three primary fluid ports completing the mechanical assembly. These needles maintain the chamber's fluid seal and provide effective means for connecting the quadrupole chamber to the dielectrophoresis fluid circuit of Figure 18.

Setup of the Experimental Fluid Circuit

An important element of the experimental system turned out, in the end, to be the fluid circuit. Its impact on particle delivery, bubble elimination and experimental repeatability was of paramount importance to the success of the project. Early chamber designs were primarily plagued by seal related problems, effectively rendering them useless. Second generation chamber designs, while having addressed the sealing problem, met with failure for their awkwardness pertaining to establishing electrical contact and particle injection. The union of the IC lead carrier assembly with the fluid circuit virtually eliminated all of the aforementioned problems:

- sealing the chamber was straight forward and reliable
- the IC lead frame provided a simple and robust mechanism for electrically contacting the quadrupole chiplet
- the mechanical microscope stage was easily modified to include a 40-pin DIP IC socket making repeated chamber insertion and removal straight forward
- the chamber housing with its precision aligned injection microtubule made delivery of particles into the quadrupole region simple.

The final steps to prepare the system for use were connection to the fluid circuit and filling. At the heart of the fluid circuit of Figure 18 is the fluid integrated circuit chamber (detailed in Figure 16). Four ports interface to the fluid circuit: two directly through

valves 1 and 2, and two more splitting from the 3rd chamber port via a 3-way stopcock. Tubing connected to valve 2 and stopcock ports A & B all are terminated with millipore microparticle filters immersed in the bulk source reservoir. Tubing connected to valve 1 is routed through a Gilson Minipuls-2 bidirectional peristaltic pump which returns fluid to the waste reservoir through a funnel filter.

To fill the chamber, a procedure similar to that outlined below must be followed. Valves 1 and 2 are opened with valve 3 closed and the Gilson pump is allowed to draw from valve 1 (the Fill/Flush Port in Figure 16). Once the tubing which sources valve 2

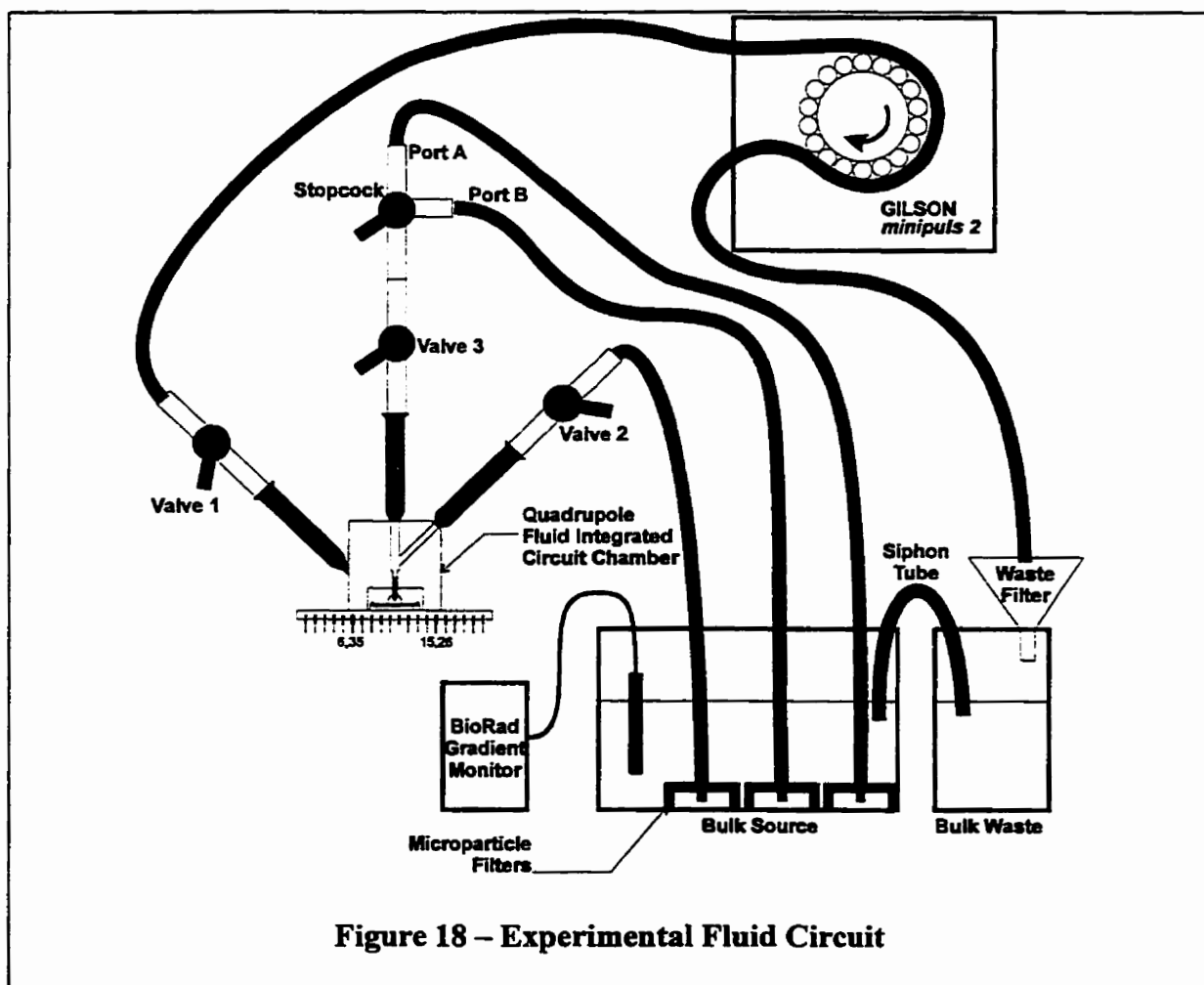


Figure 18 – Experimental Fluid Circuit

has been primed with fluid from the bulk reservoir, valve 2 is closed and valve 3 is opened with the stopcock set to connect one of its ports to valve 3. Once the first stopcock source tube has been primed, the stopcock is switched to the neighboring position to allow the second stopcock tube to be primed. With the chamber now in hand, the elimination of bubbles from the various tubings and the inner chamber cavity can be done within minutes in a fashion similar to the removal of bubbles from a partly filled syringe. Various permutations of the above cycle may need to be repeated to eliminate all the system bubbles, but once purged, the closed hydraulic system was very resistant to bubble formation.

Particle Capture

For experimentation to proceed, stopcock port A is isolated from valve 3 and a droplet containing a small number of particles is introduced through the top of stopcock port A. A hose clamp temporarily pinching the source tube to stopcock port A allows the tubing to be removed at port A, a small amount of fluid (containing test particles) to be injected and the hose connection to again be made to stopcock port A without jeopardizing seal integrity. Valves 1 & 3 are then opened, and valve 2 closed. The stopcock is set to connect port A to valve 3, and the pump is enabled at its lowest flow rate ($\sim 10\mu\text{L}/\text{min}$) to assist the migration of the injected particles down the injection tube and into the quadrupole region. Determining when particles have reached the quadrupole region is accomplished by monitoring the image from the Javelin video camera mounted to the microscope. The placement of the chamber in the microscope's primary optical path is shown in Figure 19. Once a particle has emerged from the tip of the microtubule, the pump is switched off and all three valves (1,2 & 3) are closed to completely isolate

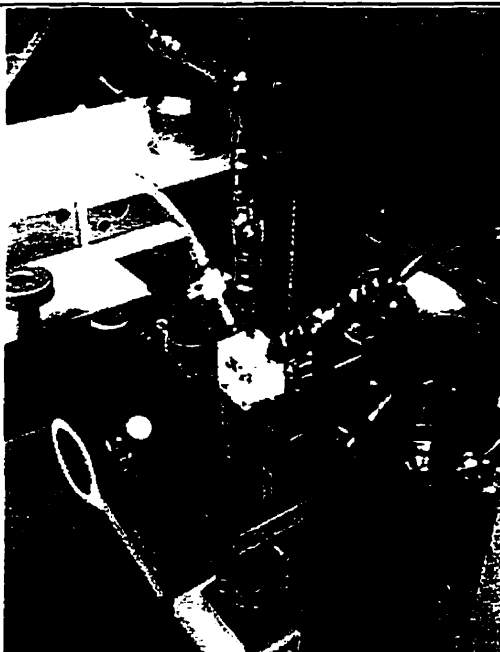


Figure 19 - Quadrupole Chamber Mounted in Optical System

the interior chamber from external disturbances. A bit of patience, a touch of luck and a much practice enables the particle injection system to perform very well: particles can be captured and flushed from the system via the fluid circuit quickly, reliably and repeatably.

Hydrodynamic Particle Rolling

Images obtained by the microscope's view of the inner chamber were captured by the video camera and fed directly to a black and white tabletop monitor to serve as feedback during the particle capturing phase of the experiment. Often a particle could be seen to have entered the chamber only to fall to the substrate outside of the quadrupole



Figure 21 - Fluid Circuit Hydro Dynamics

Levitation Data

Once a particle has been delivered into the quadrupole region, levitation data including the applied voltage, particle radius and levitation height could be collected.

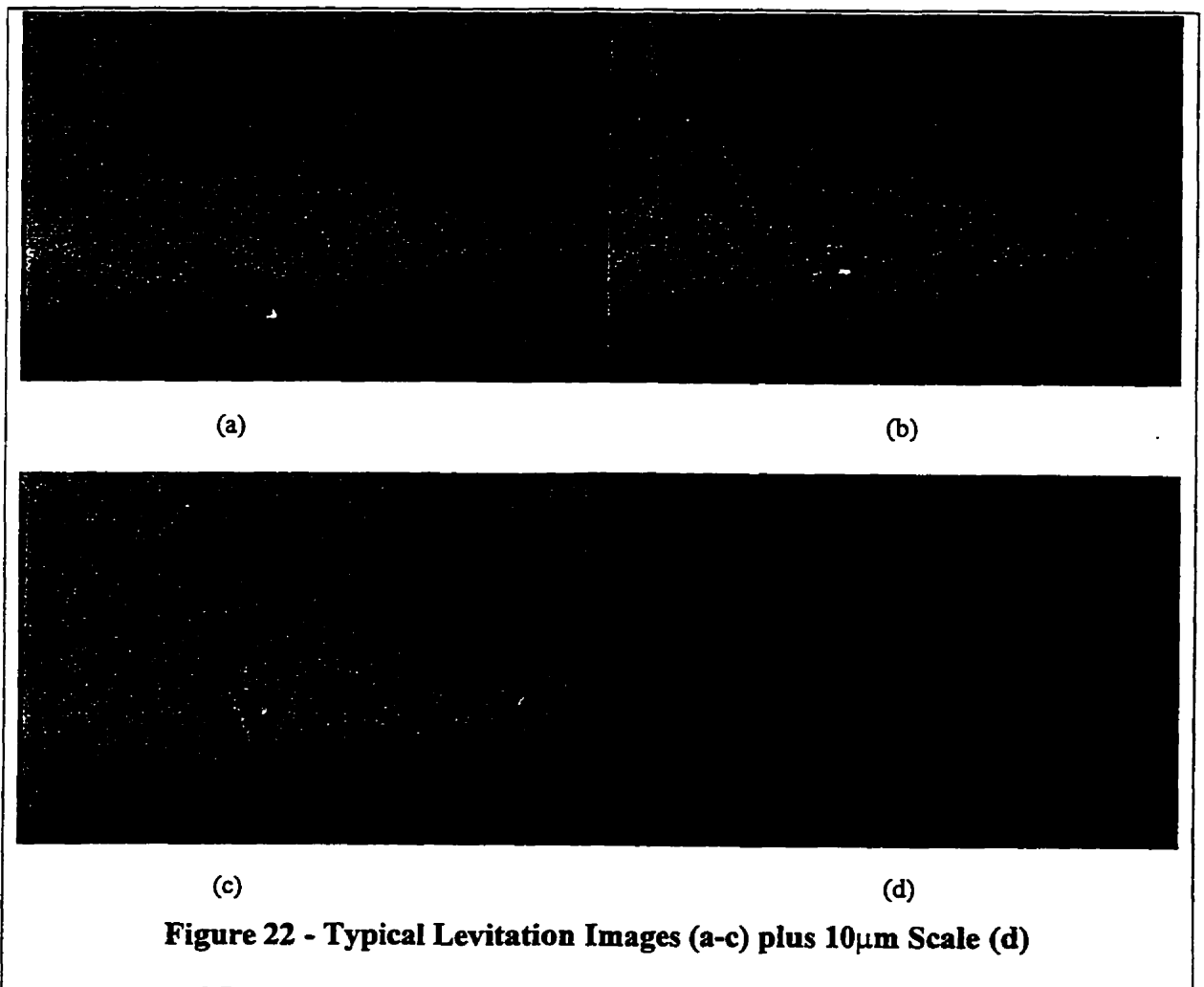
Instrumentation, electronics and measurement equipment used included the following:

- Data Precision 3500 R.M.S. meter
- Hewlett Packard 8116 Function Generator
- Leitz-Wetzlar Inverted Microscope
- Javelin JE2362A TV Camera
- Matrox MVP-AT Image Processor Card

- High Voltage Regulated Power Supply (Heathkit Model IP-17)
- Biorad Model 1710 Gradient Monitor
- 4 Output Dual Phase Amplifier Board

These items are identifiable in Figure 13 on page 45.

Figure 22 (a, b & c) depict three sample images typical of those attained during levitation experiments on polyethylmethacrylate beads. In these images the electrodes are visible in cross section below and to both sides of the trapped particle. Recall the optical system is looking across the short axis of the quadrupole chiplet of Figure 14



(Page 46). These images were captured using the Matrox image processing equipment and Figure 22d (a geometric scale in $10\mu\text{m}$ divisions) was superimposed on the particle images to allow vertical height information to be measured.

As stated previously, the goals of the quadrupole levitation experiments were to demonstrate an r^5 dependence in the quadrupole force as predicted by multipolar moment quadrupole theory and to demonstrate the utility of boundary element simulation as a tool for dielectrophoretic system design. To achieve these goals, two species of particles were used: Spheriglass[®] Soda lime beads from Potters Industries and polyethylmethacrylate beads from Bangs Laboratories. The physical specifications of these particles are given in Table 1.

	Material	
	Spheriglass	Methacrylate
ϵ_p	6.9	2.75
K_2 (in water)	-2.88	-3.15
$\delta_p(\text{kg/m}^3)$	2200	1100

Table 1 - Properties of Levitated Particles

All experiments were carried out with sinusoidal voltages at 100kHz. In the section dealing with the boundary element simulation results, it was mentioned that all simulations were run in DC-static permittivity mode. While the dielectrophoretic polarization phenomenon is a frequency dependent effect, the present capabilities of Coulomb to compute an electrical body force is limited to the DC case. While this is a shortcoming in the capabilities of the present simulator version, it was aptly suited for studying the characteristics of homogeneous spheres in ultra low conductivity media.

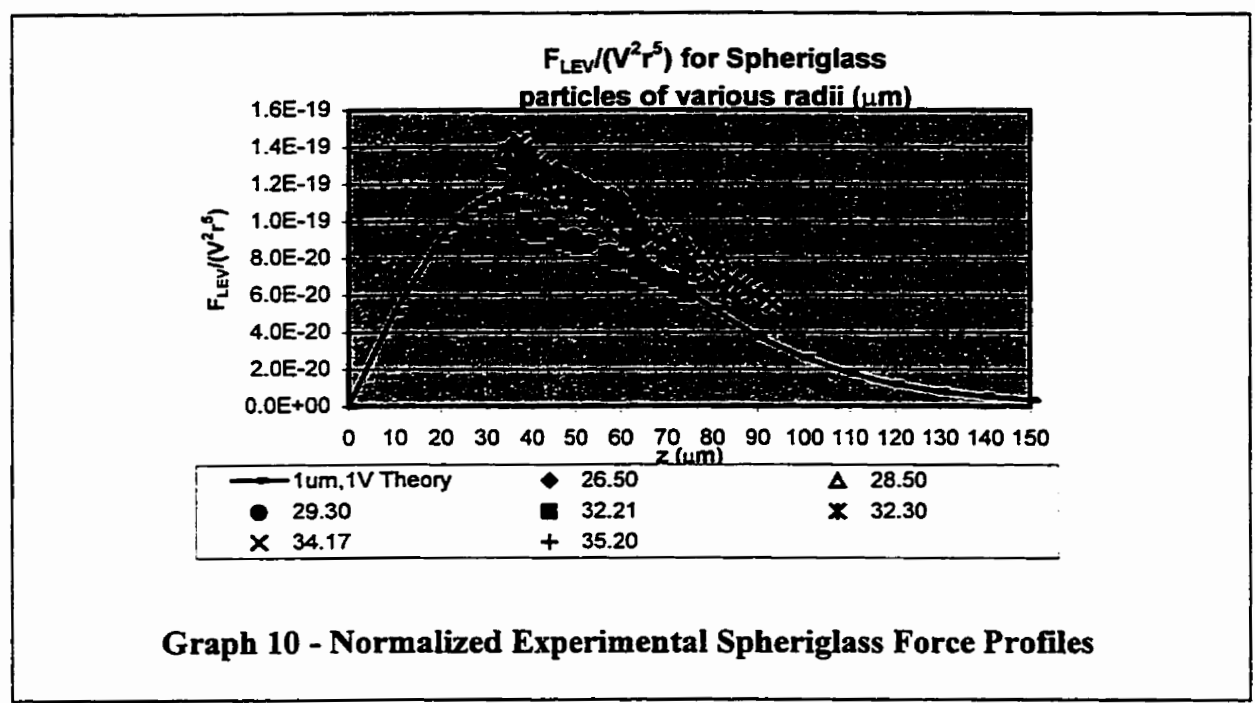
Water deionized with a NANOpure® filtering system was used, and the media conductivity was consistently observed between 1.5-2.5 μ S/cm.

On data collected from several particles of both species, two fundamental transformations were repeatedly performed to fit the experimental data to theory. The first transformation sought to produce the theoretical quadrupole force profile from the experimental data. For each particle observed, the density of water, the density of the particle and the particle's radius (measured optically) were used to compute the net gravitational force on the sphere. At any stable levitation point, this force must be equal and opposite the dielectrophoretic force being applied by the electrode system. At any point of levitation therefore, the magnitude of the dielectrophoretic force could be taken to be constant and equal to the net gravitational force (taking buoyancy into account).

Varying the applied voltage had the anticipated effect of altering the height of stable levitation, but normalization for this voltage dependency is possible by dividing the known levitation force by the square of the applied rms voltage. The resultant should be the dielectrophoretic force that the observed particle would experience when manually placed at the same points through the vertical region of interest with the quadrupole biased at a constant $\pm 1 V_{\text{rms}}$.

An additional factor expected to affect the force profile is the radius of the particle to the 5th power. To thereby normalize the experimental data obtained from particles of several different radii, the voltage normalized force data from above is further transformed by dividing the radius (in microns) to the 5th power into each of the voltage normalized force values. The experimental radius was measured optically using the geometric scale of Figure 22d. This data, now normalized for voltage and radius, when

plotted against the vertical height should match the theoretical dielectrophoretic force that a 1 μm radius particle of the same material would experience if translated through the same vertical region over the discrete electrode quadrupole biased at $\pm 1V_{\text{rms}}$. A force profile such as this was previously acquired via boundary element simulation and was



used to derive the point charge quadrupole configuration best fitting the discrete planar profile.

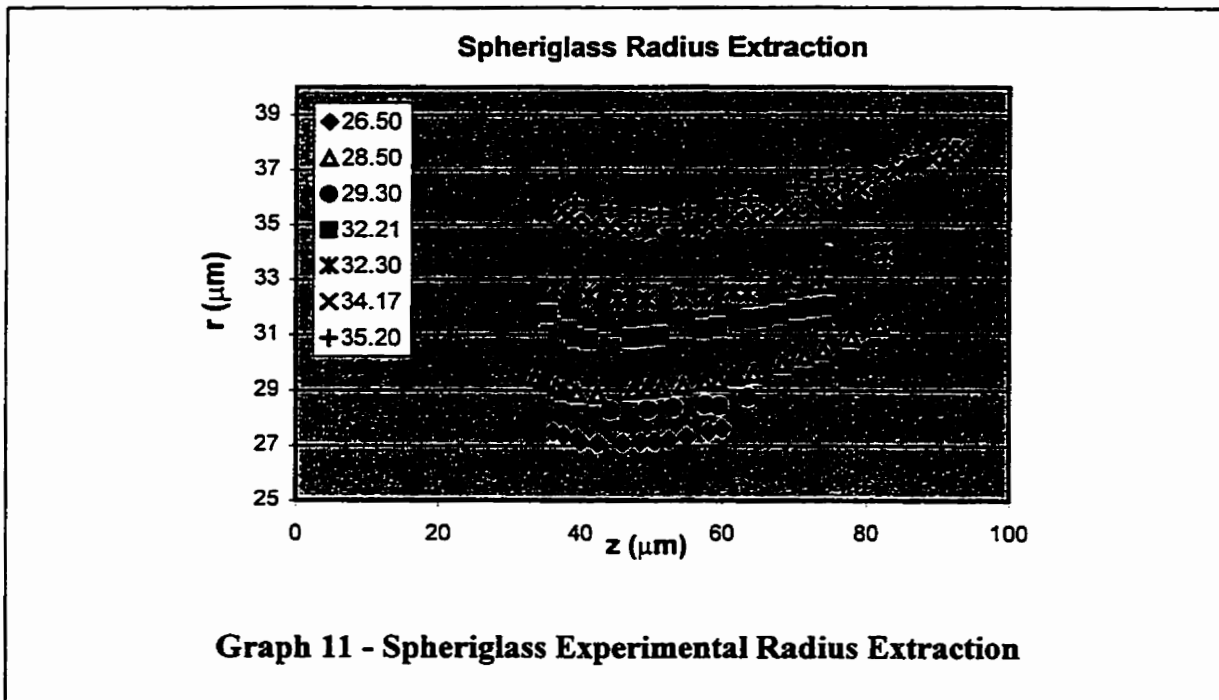
In Graph 10, the normalized levitation data for seven Spheriglass particles, ranging in radius from 26.5 μm to 35.2 μm , is plotted along with the $\pm 1V$, 1 μm force profile expected from the equivalent point charge quadrupole. The agreement between the normalized data and the theoretical prediction in Graph 10 suggests that multipolar

moment quadrupole theory is indeed sound and also stands to validate the the boundary element technique used to model the discrete planar quadrupole.

Another key observation pertaining to Graph 10 is that no particles were observed levitating below approximately $35\mu\text{m}$ as would be expected. Points along the theoretical force profile between $z=0$ and the height of the force maxima are not capable of stable levitation. In the absence of a negative feedback system, particles in this region experiencing a force sufficient to overcome the force of gravity would find themselves raised past point of the force maxima. The particles would reach a passively stable levitation point on the downward sloping section of the curve where the dielectrophoretic force exactly balances the gravitational force.

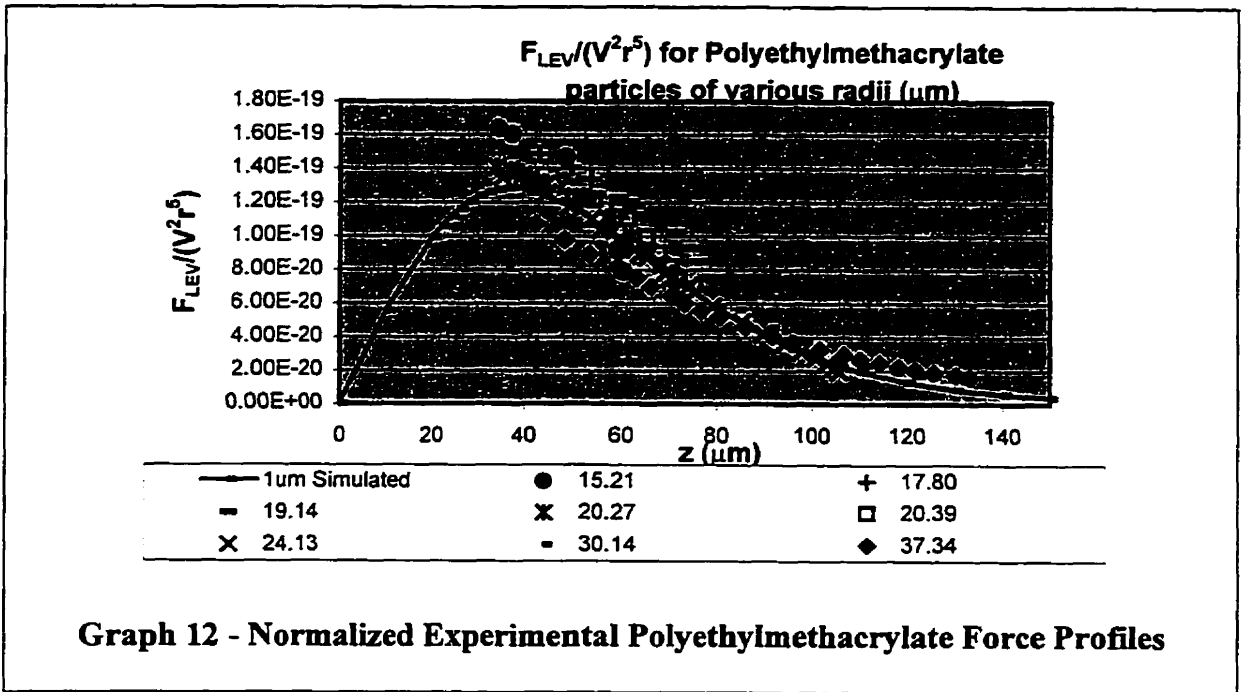
Another informative way to view the Spheriglass levitation data is to subject the data to a radius extraction transformation. Radius extraction was first used on the boundary element simulation data to attempt to verify the r^5 dependence of the quadrupole's dielectrophoretic force. This method begins by taking the net gravitational force exerted on the object as being equal to the dielectrophoretic force at any point of stable levitation. Then, for each data point, the anticipated force on a $1\mu\text{m}$ Spheriglass particle at the same vertical position is calculated by scaling up the characteristic $\pm 1\text{V}$, $1\mu\text{m}$ curve by the square of the applied voltage as per Equation (38). This yields the force expected on a $1\mu\text{m}$ particle positioned at the observed height with the quadrupole biased at the observed voltage. Next the net gravitational force on the observed particle is divided by the corresponding expected dielectrophoretic force on a $1\mu\text{m}$ particle, and

the 5th root of the result is taken. Ideally, the results plotted against the z-axis location would be a set of flat lines at the radii of each of the particles observed.



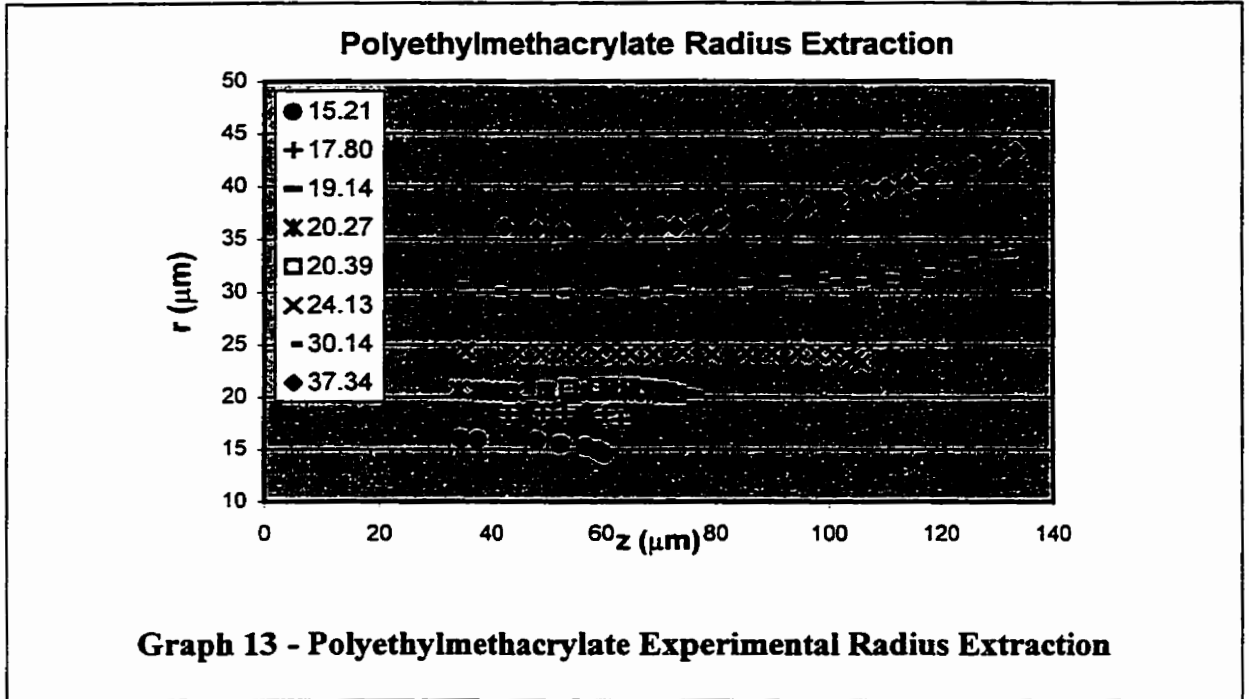
This radius extraction transformation on the Spheriglass levitation data is presented in Graph 11. While the curves are not exactly flat, they do confirm the existence of an r^5 dependence in the observed data. During levitation of the Spheriglass particles in particular, due to their high density, the voltages required for levitation reached the limits of the amplifier. At these voltages, fluid turbulence presumably due to conductive heat generation between adjacent quadrupole electrodes was visible. Such fluid disturbances would presumably have created an upward fluid flow acting to assist the dielectrophoretic force in levitating the particle. Particles therefore observed levitating at slightly higher levels than the observed voltage and radius would have predicted would have occurred. The above radius extraction algorithm applied to

particles being subjected to such fluid assisted levitation would predict radii slightly greater than the observed value, as tends to be the case in Graph 11. Additionally, the fluid turbulence was observed to be stronger for higher voltages. This would support the upward sloping tendency of the radius extraction curves for particles levitated at greater z-heights requiring greater applied voltages and therefore stronger fluid turbulence.



In a manner identical to that for the Spheriglass particles, levitation data for a set of polyethylmethacrylate beads was gathered and similarly processed. These beads, much less dense than the heavier Spheriglass beads, allowed for levitation about a much greater vertical range. Graph 12 depicts the results obtained after normalizing the levitation data to the $\pm 1V$, $1\mu\text{m}$ force profile where it can be seen that levitation in the tail of the profile

was attainable. This transformation and the radius extraction data of Graph 13 provide additional evidence suggesting that multipolar moment quadrupole theory is in fact valid.



Sources of Error

While the experimental data was sufficient to lend evidential support to multipolar moment method quadrupole theory, some comments pertaining to experimental error are justified. For the Spheriglass particles in particular, the largest anticipated sources of error arose from two factors: power amplifier distortion at high voltages (leading to potentially questionable rms voltage readings), and thermal disturbances in the media due to these high voltages generating Joule heating in the media (resulting in upward convection). At higher applied voltages, the linear region of the amplifier used to

amplify and invert the signal generators input began to show signs of distortion whereby deviations from pure sinusoidal appearance were evident when observed on an oscilloscope. The effect was not destructive to the levitation phenomenon, but an amplifier capable of reliably producing more stable sinusoidal voltages throughout the amplitude range required would have been beneficial. As for Joule heating, the Spheriglass radius extraction data demonstrated less stability than that for the polyethylmethacrylate beads. The latter beads, being much less dense and slightly more polarizable (larger K_2 value), could be levitated at identical heights as same-sized Spheriglass particles, but with much lower voltages. With less voltage being applied, less heating would occur and convection disturbance effects would similarly be reduced. This supports the more stable radius extraction results obtained for the polyethylmethacrylate beads.

At higher voltages, the dual phase amplifier used to create the inverse quadrupole voltages began to demonstrate slight imbalances in the measured rms voltage between the two phases. Identified late in the experimentation phase, the problem was not addressed numerically, and remains as an issue that should be considered in any future work. It is suspected that the imbalance would result in an optimal equivalent quadrupole not entirely charge balanced, but rather exhibiting a slight offset (ΔQ) between the two polarities of charges in the point charge model, but such an imbalance was not characterized numerically to address its effect.

Vertical height measurement, another possible source of error, was minimized through the establishment of the horizontally viewed levitation environment. Prior art [10], reported a quadrupolar size effect from a vertically aligned optical system

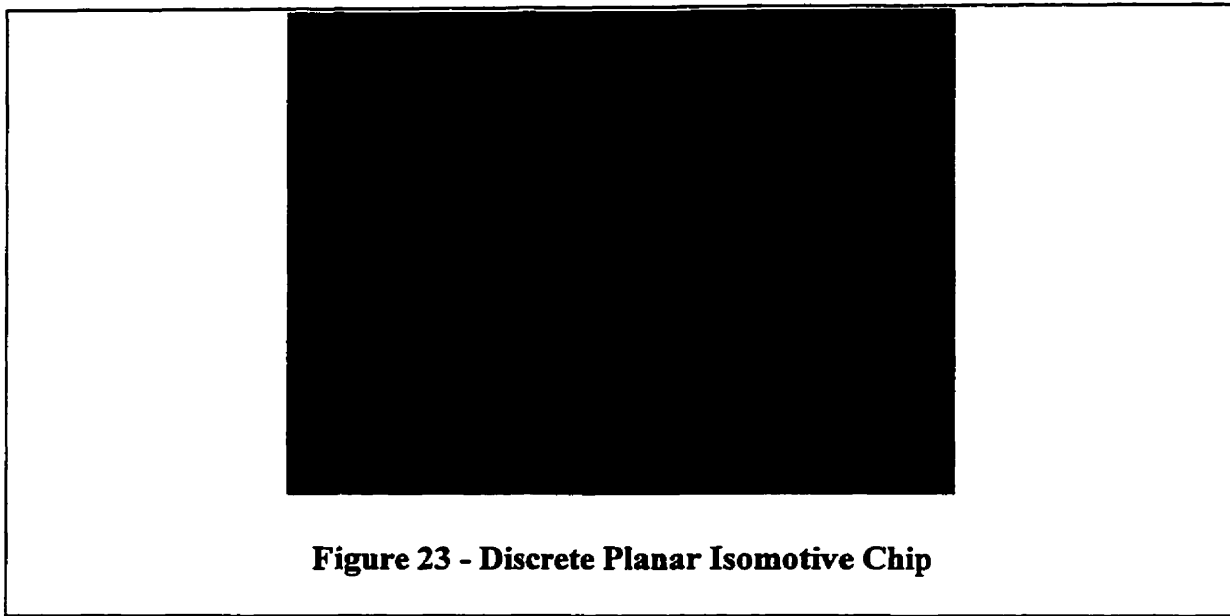
positioned over an active quadrupole region. Detecting vertical displacements this way would be much more prone to errors. The horizontally viewed system in the present work allowed for reliable detection of the particle's centroid position easily. Early experiments however, prior to the final implementation of the experimental fluid circuit, suggested that stable levitation was occurring in the region of the force characteristic predicted by theory to be unstable. As was learned, this offset was determined to be an optical effect due to the method used to determine the zero-height reference. With the introduction of the experimental fluid circuit, the substrate in front of and behind a levitated particle was easily kept free of obstruction due to other particles. Consequently, the reliability of the vertical displacement data was greatly enhanced.

CONCLUSIONS

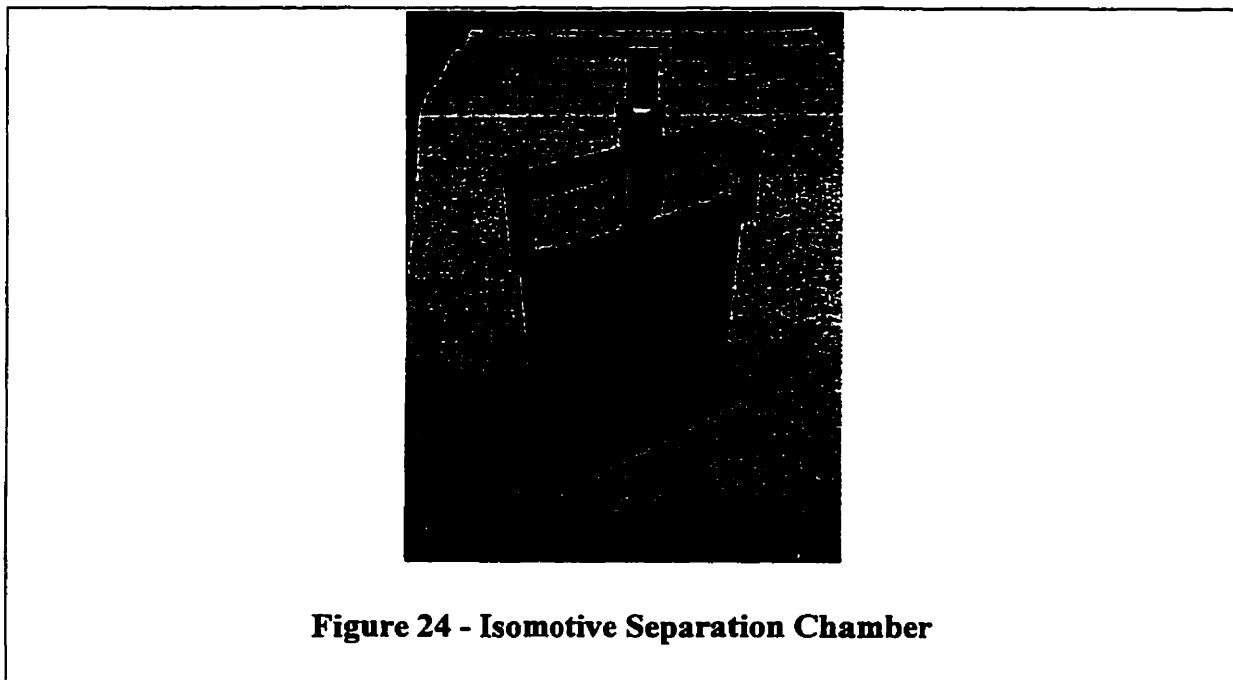
Summary of Accomplishments

Numerical simulation and experimental observation on model particles have been united to offer strong evidence supporting the validity of multipolar moment quadrupole theory. The design, construction, assembly and test of a discrete planar electrode quadrupole chamber facilitated the experimental verification of this theory by confirming the predicted size dependence on the quadrupole force characteristic. The perilous step of putting one's faith in a software simulator has been made more certain through the application of a triple stage verification procedure: numerical simulation of analytical theory, numerical simulation of discrete planar approximations and experimental verification confirming the equivalence of all three.

An effective fluid integrated circuit system was developed which allowed for flexible and reliable particle manipulation to and from the enclosed electrode system. The system was built around a standard integrated circuit lead frame. It offered an excellent mechanism for making electrical contact with the outside world. A reliable fluid seal was easily achieved while maintaining the ability to dynamically fill the system, inject particles, levitate particles and subsequently flush the system. The need to perform time consuming chamber disassembly, cleaning, reassembly, and refilling was minimized as uninterrupted cleaning procedures were made possible via the experimental fluid circuit's various pumping capabilities.



Although not experimentally characterized at the time of publication, the discrete planar isomotive structure characterized numerically in the present work was fabricated at the Alberta Microelectronics Center. Results are expected in the coming months on the



ability of the device to separate species of biological cells according to their frequency dependent polarizabilities. The planar device, shown in Figure 23 is paired with an identical device biased with voltages of opposite polarity and housed in the chamber system of Figure 24. The system fully integrates fluid and particle delivery, observation windows and electrical biasing.

Problems Encountered

As stated, a primary goal of the work was to demonstrate the validity of boundary element simulation techniques to the characterization for theoretical modelling of discrete electrode configurations. Initially, this phase of the work was hindered by an algorithmic bug in the Coulomb software whereby the magnitudes and directions of electrical body forces calculated by the program were in disagreement with fundamental electrostatic theory. Considerable effort was put to addressing this problem and working with the creators of the program (Integrated Engineering Software, Winnipeg) to resolve the problems. The program was eventually corrected and extensive boundary simulation of the discrete planar dipole, quadrupole and isomotive structures were undertaken. The performance of the simulator was, in the end, exemplary within a particular scope. That scope is limited to the case of DC permittivity analysis only. In the case of media and particles possessing non-zero conductivities, the frequency dependent nature of the dielectrophoretic phenomenon cannot be handled by Coulomb in its electrical body force calculations. Similarly, conductivity contributions due to ionic concentrations presently have no means for representation in Coulomb. It is therefore impossible to address issues such as electrode polarization effects with the current simulator.

Unrelated to the simulation problems, mechanical difficulties involved in achieving horizontal viewing of quadrupole levitation was underestimated. A total of three permutations of chambers were designed, built and unsuccessfully tested before the integrated circuit lead frame carrier was adopted into the design along with the precision aligned particle injection microtubule. The latter configuration, coupled to the external fluid circuit, allowed for quality experimental results to be obtained. Regrettably, the timing of this experimental setup's completion left enough time only to characterize the effect of the planar electrode quadrupole on homogeneous spherical particles in ultra-low conductivity media. That scenario, fortunately, is the same scenario manageable by the boundary element simulator. Consequently, the original goal of correlating analytical, numerical and experimental data was achieved.

Directions for Future Work

As mentioned, the boundary element simulation tool (Coulomb) lacks the computational ability to tackle applications representative of microbiological systems. Recent work by Dr. R. Paul and Dr. K.V.I.S. Kaler at the University of Calgary have begun to address the effects of ionic media on dielectrophoretic behavior. Their work, termed electrode polarization, is a Green's function methodology similar to the fundamental algorithm of the boundary element method. Admittedly, the development of a full-featured 3D electrostatic simulator similar to Coulomb, but possessing the ability to handle AC frequency, conductivity and electrode polarization effects in its force calculations would probably not be feasible. However, a collaborative effort between the staff at Integrated Engineering Software and the theoreticians at the University of Calgary may be feasible whereby theoretical work pertaining to electrode polarization

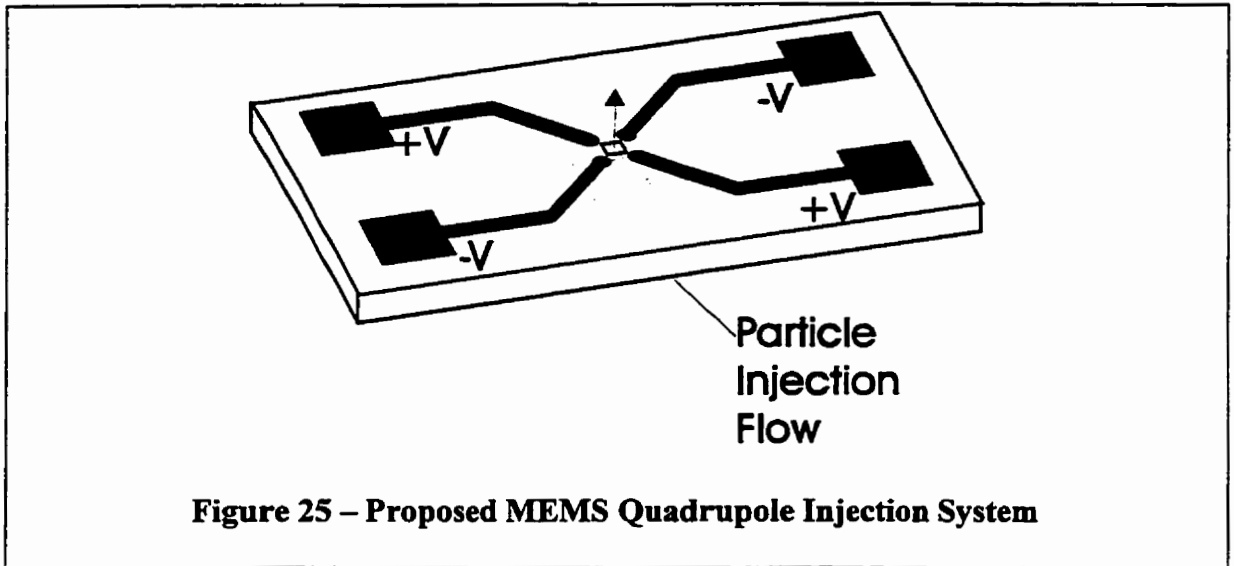
phenomenon is integrated into the existing Coulomb solver. The result would be a profoundly more capable product for Integrated Engineering Software to market and the availability of a powerful tool for dielectrophoretic researchers to use in modelling increasingly complex dielectrophoretic biological particle processors.

To offer experimental validation to such an effort, characterization of the discrete planar quadrupole levitation system with its demonstrated ease of operation and reliable ability to measure levitation profiles should be continued. While possibly requiring insulating passivation of the electrodes in the presence of highly conductive biological media, horizontal quadrupole levitation of biological cells should be performed to study their frequency dependent dielectrophoretic responses. Similarly, the discrete planar quadrupole may prove to be a valuable tool for experimental study of electrode polarization phenomenon at lower frequencies in the negative DEP spectrum of biological cells. Again, for this work to proceed, numerical methods able to model the hypothesized electrode polarization effect for the discrete planar electrode geometry must first be developed.

The emergence of microelectromechanical systems (MEMS) methodologies in recent years have been dominated by passive structures. In many cases this has been due to the difficulties of maintaining traditional microelectronics function throughout the course of many MEMS processing cycles. Many chemicals used to etch channels and holes end up making sacrificial layers out of insulators and metals required for a conventional integrated circuit function. Leaders in the MEMS arena must inevitably confront these issues if the technology is to permeate the world of consumer and industrial electronics.

This work was not meant to pioneer those breakthroughs in MEMS technology that will allow fluid integrated microcircuits with on-board electrode biasing networks to become an immediate reality. Instead, methodologies and motivations for preparing dielectrophoretic applications in advance of that day were concentrated on. Planar surface electrode arrays with underlying field programmable active bias networks would enable devices to dynamically reconfigure their dielectrophoretic function for the particular task at hand. A planar processor may take on an isomotive appearance to migrate particles across the substrate to a desired location. The field topography may then adapt itself into a quadrupolar configuration thereby allowing particles to be raised from the surface for subsequent capture by fluid systems on different vertically stacked levels.

While such systems are not possible with the present state of technology, one device which would inevitably find its way into such highly integrated systems is within reach today, and would be well worth experimental study. The MEMS quadrupole injector system illustrated of Figure 25 requires only single layer metalization of the discrete planar quadrupole electrode pattern onto a silicon substrate through which a central hole has been chemically etched. As was discussed, many of the difficulties associated with the quadrupolar levitation in the present work were eventually solved by the relatively complicated combination of the particle injection system and the experimental fluid circuit. A much more elegant mechanism for particle injection would allow the particles to precisely enter the quadrupole region not from above the plane of the quadrupole, but directly through the substrate from below.



Alternatively the device could be used in a top-loading particle configuration (as in the current embodiment), but with the chamber system modified to allow fluid to be drawn from the sealed inner chamber out through the etched hole. Now particles entering the chamber from above the quadrupole would be hydrodynamically focussed into the quadrupole region and may be gated from passing through the hole in the substrate (and hence out of the chamber) by the application of a voltage sufficient to keep them levitated in inner chamber. The function of the device in this mode reminds one of a plunger valve.

The scope of applications available to researchers and designers in the coming years will be dictated largely by the rate at which advances are made in MEMS technology and the directions in which those advances are made. As with any technology, necessity is the mother of invention, and a continued pursuit of the experimental limits of dielectrophoresis is necessary to ensure the field keeps pace with MEMS technology; thereby demonstrating necessity. MEMS activity in the biological engineering sciences

is becoming increasingly prevalent, and with that industry's close affiliations with the medical, pharmaceutical and microbiological industries, it is natural to expect that this growth is sustainable and that significant rewards are attainable.

APPENDICES

Mechanical Drawings

CHAMBER STAGE FRONT ELEVATION

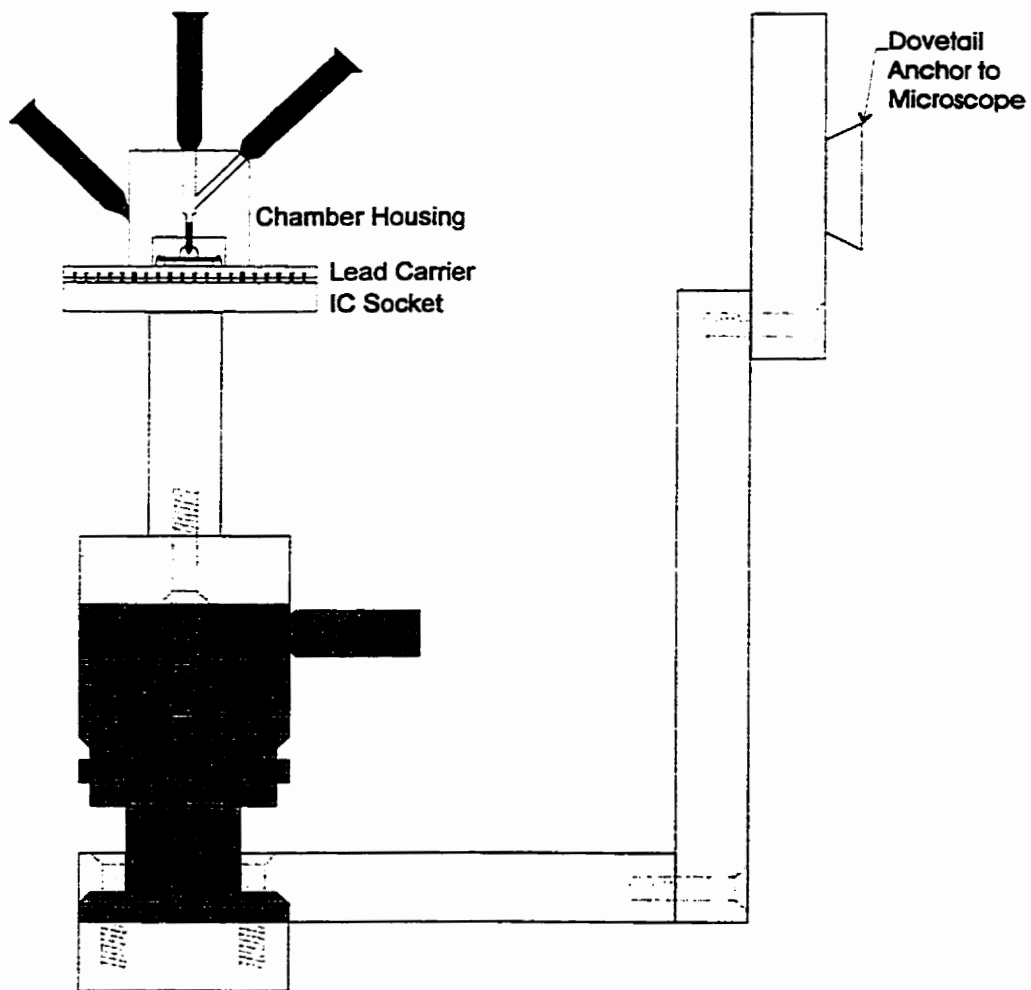


Figure 26 - Front View of Microscope Chamber Stage

CHAMBER STAGE SIDE ELEVATION

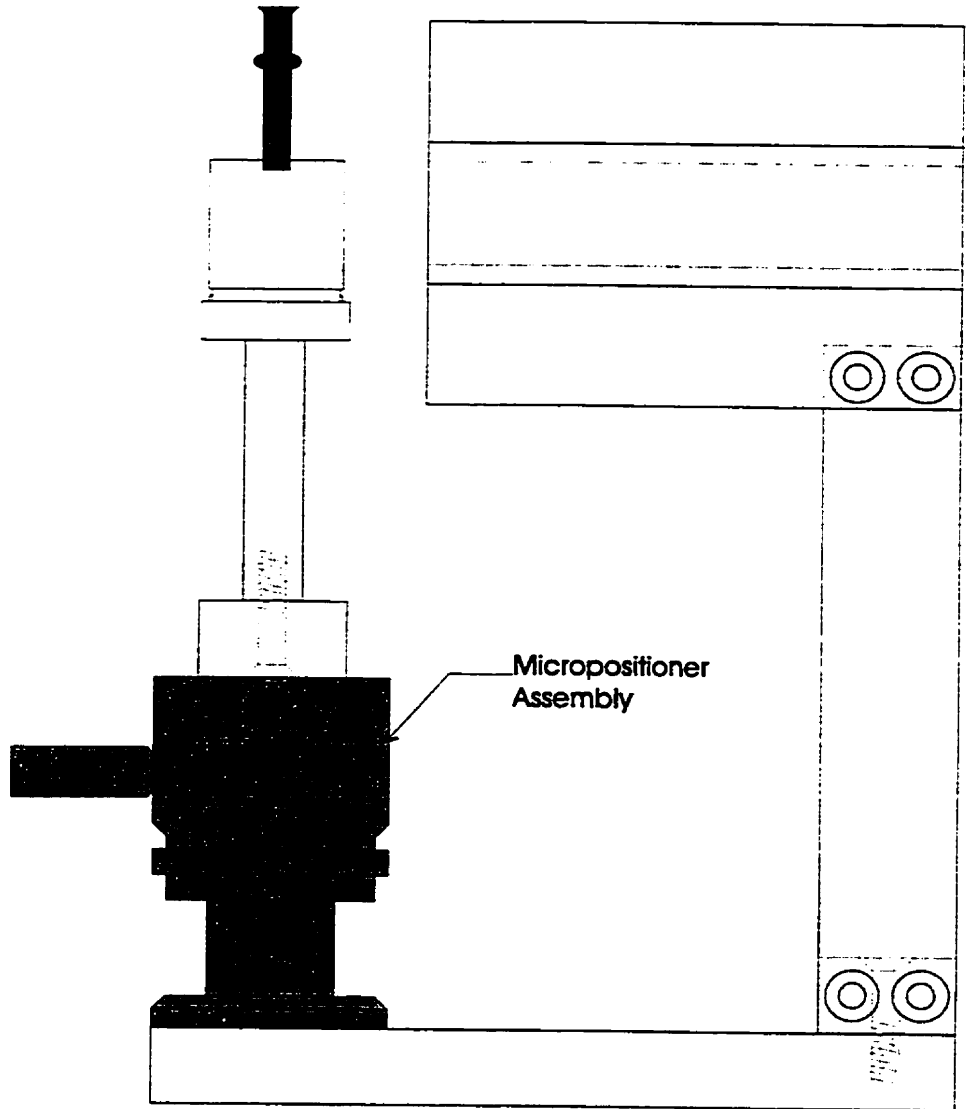


Figure 27 - Side View of Microscope Chamber Stage

EALING OPTICS MICROPOSITIONER ASSEMBLY Front Elevation

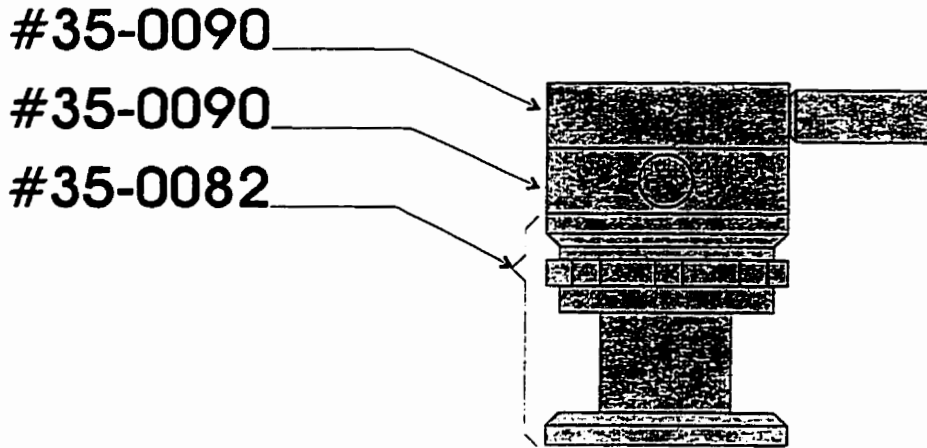


Figure 28 - Ealing Optics (x,y,z) Adjust Assembly

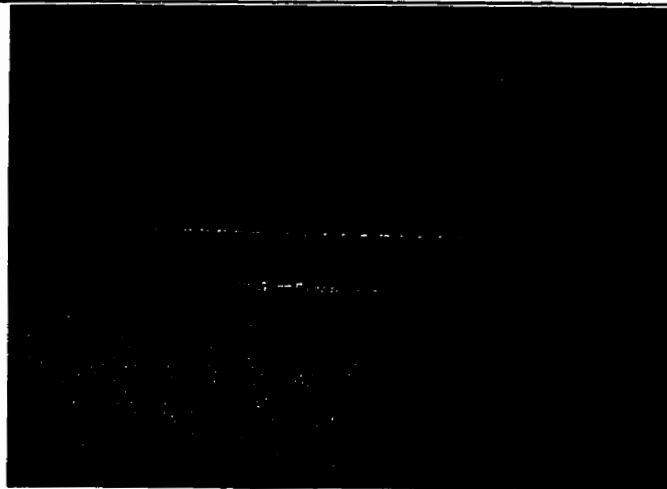


Figure 29 - Lead Carrier Assembly Prior to Housing Attachment



Figure 30 - Assembled Chamber Housing

REFERENCES

1. H.A. Pohl, Dielectrophoresis, Cambridge University Press, Cambridge, 1978.
2. M. Washizu, T.B. Jones, "Multipolar dielectrophoretic force calculation", *Journal of Electrostatics* 33 (1994) 187-198.
3. M. Washizu, T.B. Jones, K.V.I.S. Kaler, "Higher-order dielectrophoretic field effects: levitation at a field null", *Biochimica et Biophysica Acta*, 1158 (1993) 40-46.
4. T.B. Jones, *Electromechanics of Particles*, Cambridge Univ. Press, Cambridge, 1995
5. Canadian Microelectronics Corporation, "Can-MEMS Micromachining Service Instructions", Canadian Microelectronics Center, Kingston, ON, November 1995.
6. Canadian Microelectronics Corporation, "An Introduction to Micromachining", Canadian Microelectronics Center, Kingston, ON, September 1995.
7. V. Lehmann, "The Physics of Macropore Formation in Low Doped n-Type Silicon", *J. Electrochem. Soc.* 140 (10), 1993.
8. R. Weast, *Handbook of Chemistry and Physics – 66th Edition*, CRC Press, Boca Raton, 1986.
9. H. Pohl, K. Pollock, "Electrode geometries for various dielectrophoretic force laws", *Research Note* 74, Oklahoma State University, Stillwater, September 1977.
10. G. Fuhr, "Levitation, holding and rotation of cells within traps made by high-frequency fields", *Biochimica et Biophysica Acta*, 1108 (1992) 215-223
11. G. Fuhr, Th. Schnelle, R. Hagedorn, S. Shirley, "Dielectrophoretic field cages: technique for cell, virus and macromolecule handling", *Cellular Engineering*, 47-57, Autumn 1995.
12. M. Washizu, T.B. Jones, "Dielectrophoretic Interaction of Two Spherical Particles Calculated by Equivalent Multipole-Moment Method", *IEEE Transactions on Industry Applications*, Vol. 32, No. 2, March/April 1996.
13. T.B. Jones, M. Washizu, "Multipolar dielectrophoretic and electrorotation theory", *Journal of Electrostatics* 37 (1996) 121-134.
14. R. Paul, K.V.I.S. Kaler, "The Phenomenon of Electrode Polarization in Dielectrophoresis", 1997.

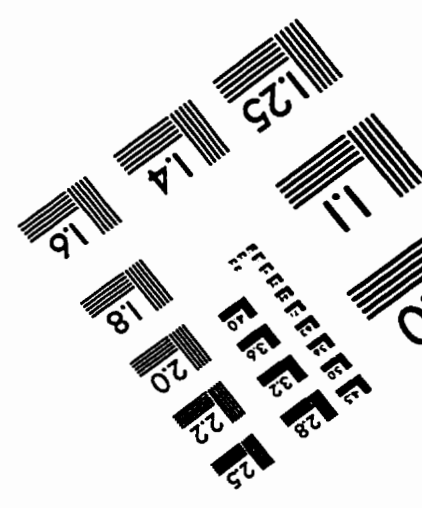
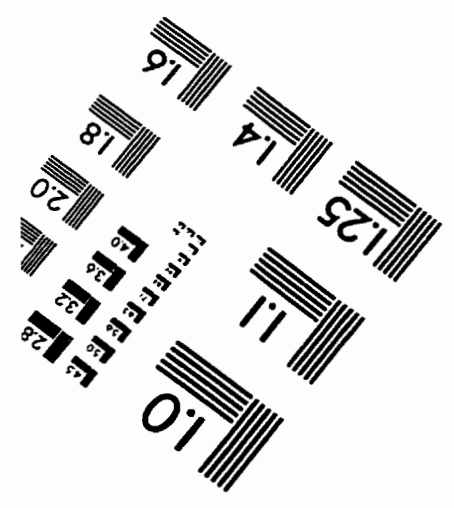
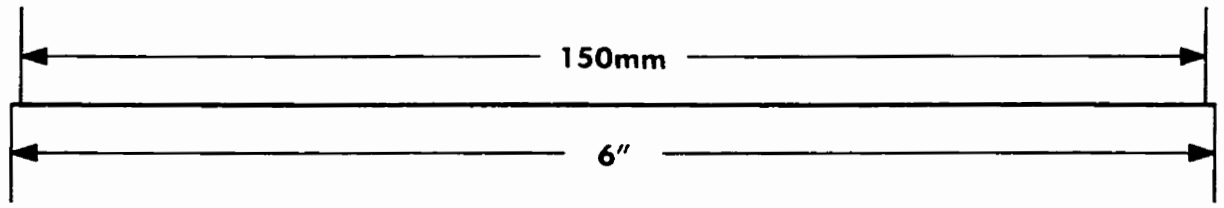
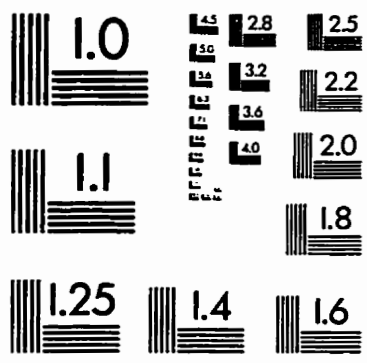
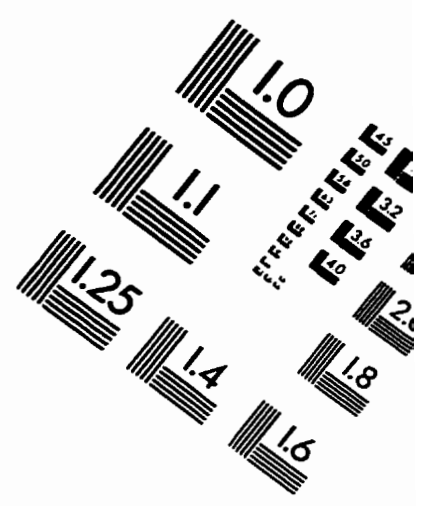
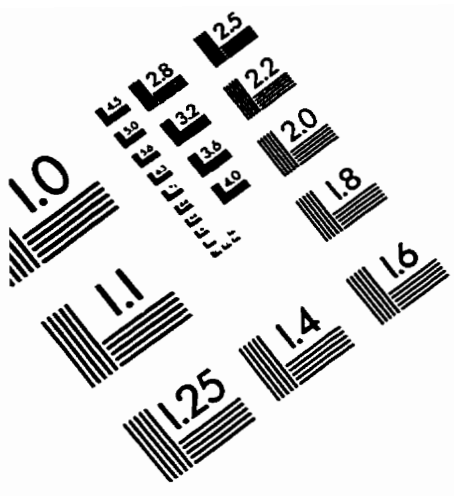
15. S. Paddison, R. Paul, K.V.I.S. Kaler, "Hysteresis loops in the low frequency region of the Clausius-Mossotti polarization factor: the result of non-linear boundary conditions at the particle interface", *Bioelectrochemistry and Bioenergetics* 38 (1995) 321-331.
16. K.V.I.S. Kaler, J. Xie, T.B. Jones, R. Paul, "Dual-frequency dielectrophoretic levitation of Canola protoplasts", *Biophys. J.* 63, 58-69, 1992.
17. S. Paddison, R. Paul, K.V.I.S. Kaler, "Low-frequency Micromotion of DEP-Levitated Plant Protoplasts", *Journal of Colloid and Interface Science* 183, 78-90 (1996).
18. G. Fuhr, H. Glasser, T. Muller, T. Schnelle, "Cell manipulation and cultivation under a.c. electric field influence in highly conductive culture media", *Biochimica et Biophysica Acta* 1201 (1994) 353-360.
19. G. Fuhr, A. Voigt, T. Muller, B. Wagner, K. Reimer, T. Lisec, "Electric-field-mediated inhibition of cell and microparticle adhesion: a new way to create bio-repellent surfaces", *Sensors and Actuators B* 26-27 (1995) 468-470.
20. M. Washizu, S. Suzuki, K. Moro, "Dielectrophoretic Filtration of Protein Molecules in a Fluid Integrated Circuit", Faculty of Engineering, Seikei University, Tokyo, 1993.
21. M. Washizu, S. Suzuki, O. Kurosawa, T. Nishizaka, T. Shinohara, "Molecular Dielectrophoresis of Biopolymers", *IEEE Transactions on Industry Applications*, 30 (4), July/August 1994.
22. K. Osapay, W. Yound, D. Bashford, C. Brooks, D. Case, "Dielectric Continuum Models for Hydration Effects on Peptide Conformational Transitions", *J. Phys. Chem.* 100, 2698-2705, 1996.
23. S. Suzuki, T. Yamanashi, S. Tazawa, O. Kurosawa, M. Washizu, "Quantitative Analysis of DNA Orientation in Stationary AC Electric Field Using Fluorescence Anisotropy", *Cont. Rec. IEEE/IAS 1995 Annual Meeting*.
24. M. Washizu, O. Kurosawa, I. Arai, S. Suzuki, N. Shimamoto, "Applications of Electrostatic Stretch-and-Positioning of DNA", *IEEE Transactions on Industry Applications*, 31 (3), May/June 1995.
25. M.A. Plonus, *Applied Electromagnetics*, McGraw-Hill Book Company, New York, 1978.
26. *Integrated Engineering Software, "Coulomb Users and Technical Manual"*, Integrated Engineering Software, Winnipeg, 1989.

27. S. Bamji, A. Bulinski, K. Prasad, "Electric Field Calculations with the Boundary Element Method", *IEEE Transactions on Electrical Insulation* 28 (3), 1993.
28. S. Knutson, M. Abdalla, R. Pixton, "PC-Based Electrostatic Field Calculation Techniques", 12th Annual Ideas in Science and Electronics Symposium, 1991.
29. O.C. Zienkiewics, *The Finite Element Method in Engineering Science*, McGraw-Hill, New York, 1971.
30. M. Jaswon, G. Symm, *Integral Equation Methods in Potential Theory and Electrostatics*, Academic Press, New York, 1977.
31. Y. Yilder, *A Boundary Element Method for the Solution of Laplace's Equation in Three-dimensional Space*, Ph.D Thesis, University of Manitoba, Winnipeg, Canada, 1985.
32. K. Foster, A. Sowers, "Dielectrophoretic Forces and Potentials Induced on Paris of Cells in an Electric Field", *Biophysical Journal*, Vol. 69, 777-784, 1995.
33. T.B. Jones, J.P. Kraybill, "Dielectrophoretic levitation of small metallic particles in insulating dielectric liquids", *J. Appl. Phys.* 60 (4), 1247-1252, 1986.
34. T.B. Jones, G.W. Bliss, "Bubble Dielectrophoresis", *J. Appl. Phys.* 48 (4), 1977.
35. T.B. Jones, "Hydrostatics and steady dynamics of spatially varying electromechanical flow structures", *J. Appl. Physics*, 45 (4), 1974.
36. H. Pohl, R. Pethig, "Dielectric measurements using non-uniform electric field (dielectrophoretic) effects", *J. Physics E: Scientific Instruments* 10, 1977.
37. K. Asami, T. Hanai, "Observations and the Phenomenological Interpretation of Dielectric Relaxation due to Electrode Polarization", *Bull. Inst. Chem. Res., Kyoto Univ.*, Vol. 72, No. 2, 1993.
38. J. Kraybill, "Digital Feedback Systems in Dielectrophoresis", University of Rochester, Rochester, 1986.
39. I. Wickelgren, "The Strange Senses of Other Species", *IEEE Spectrum*, March 1996.
40. A. Docoslis, N. Kalogerakis, L. Behie, K.V.I.S. Kaler, "Continuous Dielectrophoretic Separation of Viable Cells in High Conductivity Culture Media", University of Calgary, Calgary.
41. P. Gascoyne, X. Wang, Y. Huang, F. Becker, "Dielectrophoretic Separation of Cancer Cells from Blood", *IEEE Proceedings* 1995, 1366-1373.

42. Y. Huang, X.B. Wang, R. Holzel, F. Becker, P. Gascoyne, "Electrorotational studies of the cytoplasmic dielectric properties of Friend murine erythroleukaemia cells", *Phys. Med. Biol.* 40 (1995) 1789-1806.
43. X. Wang, Y. Huang, P. Gascoyne, F. Becker, "Dielectrophoretic Manipulation of Particles", *IEEE Proceedings*, 1358-1365, 1995.
44. X. Wang, M. Hughes, Y. Huang, F. Becker, P. Gascoyne, "Non-uniform spatial distributions of both the magnitude and phase of AC electric fields determine dielectrophoretic forces", *Biochimica et Biophysica Acta* 1243, 185-194, 1995.
45. P. Gascoyne, F. Becker, X. Wang, "Numerical Analysis of the influence of experimental conditions on the accuracy of dielectric parameters derived from electrorotation measurements", *Bioelectrochemistry and Bioenergetics* 36 (1995) 115-125.
46. X. Wang, X.B. Wang, F. Becker, P. Gascoyne, "A theoretical method of electrical field analysis for dielectrophoretic electrode arrays using Green's theorem", *J. Phys. D: Appl. Phys.* 29 (1996) 1649-1660.
47. K. Petersen, "Silicon as a Mechanical Material", *IEEE Proceedings*, Vol 70, No. 5, 1982.
48. L.M. Holmes, "Stability of Magnetic Levitation", *J. Appl. Phys.* 49 (6), 3102-3109, 1978.
49. Kwauk, *Fluidization: Idealized and Bubbleless*, Science Press, Beijing, 1992.
50. P.N. Murgatroyd, A.T. Carmichael, S.J.P. Thomas, "Improved Differential Optical Position Detector for Magnetic Suspension Systems", *Rev. Sci. Instrum.* 56 (8), 1985.
51. A.T. Carmichael, S. Hinchliffe, P.N. Murgatroyd, I.D. Williams, "Magnetic Suspension systems with digital controllers", *Rev. Sci. Instrum.* 57 (8), 1986.
52. R.J. Hill, "Teaching Electrodynamics Levitation Theory", *IEEE Transactions on Education*, Vol. 33, No. 4, 1990.
53. J.W. Beams, C.W. Hulburt, W.E. Lotz, R.M. Montague, "Magnetic Suspension Balance", *Rev. Sci. Instrum.*, 26 (12), 1955.
54. J. Xie, *Measurement of Electrical Properties of Biological Cells Using a Dielectrophoretic Levitation System*, Department of Electrical and Computer Engineering, Calgary, 1991.
55. T.B. Jones, M. Washizu, Roger Gans, "Simple Theory for the Levitron[®]", *J. Appl. Phys.* 82 (2), 1997.

56. P.R. Gray, R.G. Meyer, *Analysis and Design of Analog Integrated Circuits* – 3rd Edition, Wiley, New York, 1993.
57. R. Pethig, *Dielectric and Electronic Properties of Biological Materials*, Wiley, Chichester, 1979.
58. C.J.F. Bottcher, *Theory of Electric Polarization*, Elsevier Scientific Publishing, Amsterdam, 1973.
59. W.R. Smythe, *Static and Dynamic Electricity*, McGraw-Hill, New York, 1968.
60. E.S. Yang, *Microelectronic Devices*, McGraw-Hill, New York, 1988.
61. P. Lorrain, D. Corson, *Electromagnetic Fields and Waves*, W.H. Freeman and Co., San Francisco, 1970.

TEST TARGET (QA-3)



APPLIED IMAGE . Inc
1653 East Main Street
Rochester, NY 14609 USA
Phone: 716/482-0300
Fax: 716/288-5989

© 1993, Applied Image, Inc., All Rights Reserved